physica status solidi a
www.pss-a.com

Check for updates

Growth of Textured Chalcogenide Thin Films and Their Functionalization through Confinement

*Peter Kerres, Riccardo Mazzarello, Oana Cojocaru-Mirédin, and Matthias Wuttig**

A number of chalcogenides show a remarkable portfolio of properties, which enables a plethora of applications including thermoelectric power generation and phase change material (PCM)-based information storage. PCMs exhibit fast and reversible switching between two (typically, amorphous and crystalline) states, characterized by different optical and electrical properties. In the last decade, textured chalcogenide thin films have been investigated to develop a better understanding of structure – property relationships, improve material performance and understand how these properties change upon reducing film thickness. In this review, the present knowledge concerning the textured growth is summarized, focusing on films of GeTe, Sb_2Te_3, and GeSbTe compounds. In particular, the impact of different deposition methods, substrate surface modifications, and methods to influence film formation is reviewed. In the second part of this review, confinement effects are discussed. Surprisingly pronounced changes in atomic arrangement, that affect film properties, and device performance are presented. These changes are attributed to the unconventional bonding mechanism in these chalcogenides coined metavalent bonding, which is trongly affected by the confinement. Bonding becomes covalent-like in the two-dimensional limit, whereas Metavalent Bonding emerges for thicker films, where electron delocalization is increased This explains the pronounced property changes with film thickness.

1. Introduction

Phase change materials (PCMs) used in electronic data storage form a class of solids, which employ a fast and reversible switching between a metastable amorphous (RESET) and a stable crystalline (SET) state. To select a suitable compound for such applications, a number of prerequisites have to be fulfilled. Switching between the phases is realized by applying heat pulses to the system, either through local heaters, laser irradiation, or Joule heating through the device. The desire to have films, which can crystallize fast and reliably, but still have a high stability of the amorphous state defines the first set of requirements for the design of functional materials.[1] Furthermore, the reduction of energy consumption of the RESET process, i.e., melting and subsequent quenching of the active area is highly desirable. As the different phases need to be read out reliably, the change in the phase should be linked to a pronounced change in easily accessible properties, such as reflectance or conductance of the samples. All these requirements are met by a subgroup of chalcogenides, including GeTe, Sb_2Te_3, and GeSbTe(GST) compounds, predominantly those located on the pseudo binary line between GeTe and Sb_2Te_3.[2] Their properties in the amorphous state are similar to ordinary covalent semiconductors such as GaAs or GeSe.[3] In the crystalline phase, however, the optical reflectivity and the electronic conductivity are much higher due to a network of overlapping *p*-orbitals.[4] This unique pattern has been coined metavalent bonding (MVB) to distinguish it from metallic, ionic, and ordinary covalent bonding.[5] It is defined by the competition between electron delocalization as in metallic bonding and electron localization as in covalent and ionic bonding.[6] It is thus expected that the properties of solids with MVB will change in reduced dimensions

P. Kerres, M. Wuttig
I. Institute of Physics
Physics of Novel Materials
RWTH Aachen University
52056 Aachen, Germany
E-mail: wuttig@physik.rwth-aachen.de

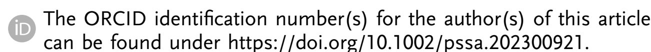
The ORCID identification number(s) for the author(s) of this article can be found under https://doi.org/10.1002/pssa.202300921.

© 2024 The Authors. physica status solidi (a) applications and materials science published by Wiley-VCH GmbH. This is an open access article under the terms of the Creative Commons Attribution-NonCommercial License, which permits use, distribution and reproduction in any medium, provided the original work is properly cited and is not used for commercial purposes.

DOI: 10.1002/pssa.202300921

P. Kerres, M. Wuttig
PGI 10 (Green IT)
Forschungszentrum Jülich GmbH
52428 Jülich, Germany

M. Wuttig
Jülich-Aachen Research Alliance (JARA FIT and JARA HPC)
RWTH Aachen University
52056 Aachen, Germany

R. Mazzarello
Department of Physics
Sapienza University of Rome
00185 Rome, Italy

O. Cojocaru-Mirédin
INATECH
Albert-Ludwigs-University Freiburg
Georges-Köhler-Allee 102, 79110 Freiburg, Germany

 © 2024 The Authors. physica status solidi (a) applications and materials science published by Wiley-VCH GmbH

such as thin films or small clusters.[7] To understand the nature and extent of the property contrast between crystalline and amorphous films, it is crucial to study trends in the crystalline state of phase change materials, to understand the limits of their beneficial bonding. This should be performed in thin films and ideally at the nanoscale to stay as close as possible to the application in highly scaled device structures, while still giving enough insight into the material properties to understand the processes involved. Commonly, thin films used to study the phase change are randomly oriented polycrystalline films. They are frequently produced by sputtering at room temperature on an amorphous SiOx surface and subsequent annealing. If such films are scaled down, the orientation distribution of grains within the film becomes more discrete and stochastic.

As most mono- and sesqui-chalcogenides show either a Peierls distortion (PD), and/or form layered structures with van der Waals like gaps in their crystal structure, the film properties often show some degree of anisotropy. The impact of this anisotropy on the film properties will also depend upon the degree of texture in the film. In addition, the effect of grain boundaries on these properties is different for high-angle, low-angle and twin boundaries.[8–10] The resulting stochasticity complicates the analysis of the underlying material properties for such thin films. Instead, producing textured films with well-defined crystallographic directions and thicknesses can overcome this issue.

Since all grains are similarly oriented, the entire film will contribute to structural information obtained in the intensity of a single diffraction peak in, for example, X-ray diffraction (XRD).[6,11,12] Using textured films can also lead to better performance in applications. Templated growth from amorphized materials either on seeds[13] or inside an epitaxially grown matrix[14] shows less crystallization stochasticity and higher crystal growth velocities, compared to (re)crystallization in randomly oriented polycrystalline materials. Since the prime goal is working with highly scaled devices, also more sophisticated growth methods than room temperature (RT) sputtering become feasible. These techniques benefit from pre-patterning of the substrate, either through selective area epitaxy[15,16] or deposition methods such as atomic layer deposition (ALD) which provide high conformity even on side walls of pre-patterned surfaces.[17]

Having a well-defined textured thin film is the prerequisite of studying how material properties and device behavior is affected by confinement. Therefore, the article is separated into two parts: Part 1 deals with different options to grow thin chalcogenide films with vapor deposition methods. This review includes the growth of (fiber and biaxially) textured films of chalcogenides. The range of substrates considered includes both single crystals and amorphous substrates. Finally, the (re)crystallization in textured samples is discussed. Subsequently, Part 2 deals with the effect of confinement on the structure and properties in ultrathin films. In contrast to the review given in ref. [7], the focus is on confinement effects for the crystalline state, with a brief summary of recent developments in PCM devices based on ultrathin films.

2. Growth of Textured Chalcogenides

Over the course of the last years, textured thin films of chalcogenide have been grown with a plethora of physical and chemical deposition methods. For physical vapor deposition, especially molecular beam epitaxy (MBE)[14,18–34] and pulsed laser deposition (PLD)[35–39] have enabled the growth of high-quality epitaxial films. These techniques can be combined with reflection high energy electron diffraction (RHEED) to monitor the film growth during deposition. Sputtering, being the workhorse of deposition techniques for dense amorphous/polycrystalline chalcogenide films at room temperature is usually seen as inferior regarding grain sizes and epitaxial alignment compared to the former two. Yet, it is more relevant for industrial applications. Nevertheless, given the right deposition conditions at elevated temperatures (about 200–300 °C), it is possible to grow high-quality textured films even with sputter deposition.[40,41] The growth with chemical vapor deposition (CVD), in the form of metal organic vapor phase epitaxy (MOVPE) and metal organic chemical vapor deposition (MOCVD), as well as atomic layer deposition (ALD) has been studied, too. With the former, a large lateral uniformity and grain sizes above 10 µm are possible,[27] while the latter recently showed device integration in crossbar structures due to the highly conformal growth even on sidewalls.[17] More details on the physical and/or chemical background of the different deposition methods can be found in the reviews of Boschker et al.[42] (PVD), Hartdegen et al.[43] (MOVPE) and Lee et al.[44] (ALD). For all deposition processes employed to form epitaxial films, the growth is improved at elevated temperatures and low growth rates of a few pm per second. The upper limit of the deposition temperature is given by the desorption of Tellurium. If the growth is performed just below this threshold, even sputtered films can show high degrees of texture, although there are still differences in film quality regarding grain size, tilt and twist of the crystallites. As all of the deposition methods used show similar film substrate interactions, the options for different substrates and terminations can be discussed together for all deposition methods covered.

2.1. Choice of the Substrate

Due to the need to adapt to semiconductor technology processes, the substrate choice is limited to CMOS-compatible substrates such as Si and SiOx. In addition, Muscovite MICA and graphene have been explored by several groups as a reference for van der Waals epitaxial growth. Al_2O_3 substrates are CMOS compatible too, but their low surface energy can cause wetting problems. First, the growth on crystalline Silicon substrates is covered: Despite the large lattice mismatch of Silicon (closest atomic spacing on (100) and (111) planes; 3.84 A[45]) and chalcogenides (i.e., GeTe 4.17 Å[46] and Sb_2Te_3 4.27 Å), GST compounds can grow quite well, especially if the surface is passivated and Van-der Waals like epitaxy is possible. The layered structure of the V_2–VI_3 and IV–V–VI compounds further enables high-quality (biaxially) textured growth. The simplest epitaxial surface for the growth on Silicon is H:Si(111), as achieved by chemical wet etching. Heating the substrate well above 700 °C will result in the formation of a 7×7 reconstructed surface, where the three top layers are reconstructed to reduce the number of dangling bonds on the surface. By depositing Sb or Bi during the cooling process, a $\sqrt{3} \times \sqrt{3}$ surface can be achieved, where the dangling bonds are passivated by adatoms of Sb or Bi, respectively.

© 2024 The Authors. physica status solidi (a) applications and materials science published by Wiley-VCH GmbH

18626319, 2024, 22, Downloaded from https://onlinelibrary.wiley.com/doi/10.1002/pssa.202300921 by Forschungszentrum Jülich GmbH Research Center, Wiley Online Library on [21/11/2024]. See the Terms and Conditions (https://onlinelibrary.wiley.com/terms-and-conditions) on Wiley Online Library for rules of use; OA articles are governed by the applicable Creative Commons License

Depending on the temperature, also other surfaces are achieved.[24,47] Hence, a precise process control is required to reliably achieve well-defined surfaces.

Regarding the texture of the films, studies of samples grown employing different deposition methods provide a coherent view. GeTe films grow on H:Si(111) with a biaxial texture with (0001) planes parallel to the surface and $\{01\bar{1}0\}$ planes along the Si {220} planes[48] (cf. **Figure 1**a). One rotational domain with a twin (epitaxial and twin) is observed, although the films have a rather large twist for epitaxial films (≈4° full width half maximum (FWHM) for MBE grown[48] and PLD grown films[37]). Contrary to the data from XRD, more local transmission electron microscopy (TEM) diffraction measurements instead reveal a fiber texture in the films.[49] Furthermore, samples deposited with an increased heating step around 350 °C show no residual fiber texture, while samples that are directly heated to the deposition temperature still show fiber texture.[18] The apparent discrepancies might be explained by the pre-processing of the samples to create the H passivated surface. In the commonly used method of etching in 1–10% HF and rinsing in DI, the surface is now passivated by the addition of H and Silanol groups on the Si surface.[50] After heating the sample above 200 °C, H_2O and H_2 will desorb slowly from the surface, creating a mixture of dangling 1 × 1 surfaces and places with remaining adatoms.

If the 7 × 7 reconstructed surface is used, the twist of the rotational domains is reduced. However, the larger surface unit cell with a lower number of dangling bonds enables the formation of additional rotational domains. The largest domain emerges at ≈7.5° offset from the Si peak, while a third domain exists at 2° offset. These maxima can be attributed to the formation of coincidence lattices with minimal misfit at the aforementioned angles.[22] On the perfect $\sqrt{3} \times \sqrt{3}$ surfaces, the films can grow with a comparable twist to the Si(111) 1 × 1 surface and only one rotational domain and its twin are present. In addition, the films grow smoother. Independent of the deposition method, the {0001} textured grains in GeTe are accompanied by a small amount of grains with $\{10\bar{1}1\}$ texture, visible as a shoulder at higher Q_z. This grain orientation appears for all substrates/surface reconstructions, as shown in **Figure 2**a. Depositing on the 7 × 7 surface can suppress the formation of these in the initial growth stage, i.e., for thinner samples. However, such grains tend to form in thicker films.[51] The tendency of this facet formation compared to other directions can be explained by the similarity of their interfacial planes, also shown in Figure 2b,d. In the high symmetry rock salt structures, the {0001} and $\{10\bar{1}1\}$ directions are equivalent to the (111) and $(\bar{1}11)$ directions. The symmetry angles in the distorted GeTe structure are 120° for the {0001} direction and 119° for the $\{10\bar{1}1\}$ directions. Nevertheless, the atomic planes are similar enough that also grains with oblique orientations can grow. The reciprocal space map in Figure 2c shows 3 domains for the oblique peaks, which can be attributed to rotational domains of the $\{10\bar{1}1\}$ grains aligned on the Si substrate.

Sb_2Te_3 films already grow with a much larger degree of in-plane texture on the Si (111) 1 × 1 surface, as shown in Figure 1b. The degree of twist is halved compared to GeTe, as the crystal structure is much better aligned to the substrate. As for GeTe, the epitaxial relation on 7 × 7 Si is more complex, showing 2 additional rotational domains at 6.7° and 16° offset, respectively.[24] In contrast to GeTe, however, the alignment parallel to the Si (110) planes is still prevalent. Similar behavior as for Sb_2Te_3 can also be found for Ge–Sb–Te films,[27,29,35,52,53] which also grow in a layered fashion. Similarly, Bi_2Se_3 grown on $\sqrt{3} \times \sqrt{3}$ Bi:Si surfaces yields smooth films with high crystalline quality.[23] In the out-of-plane direction of the layered

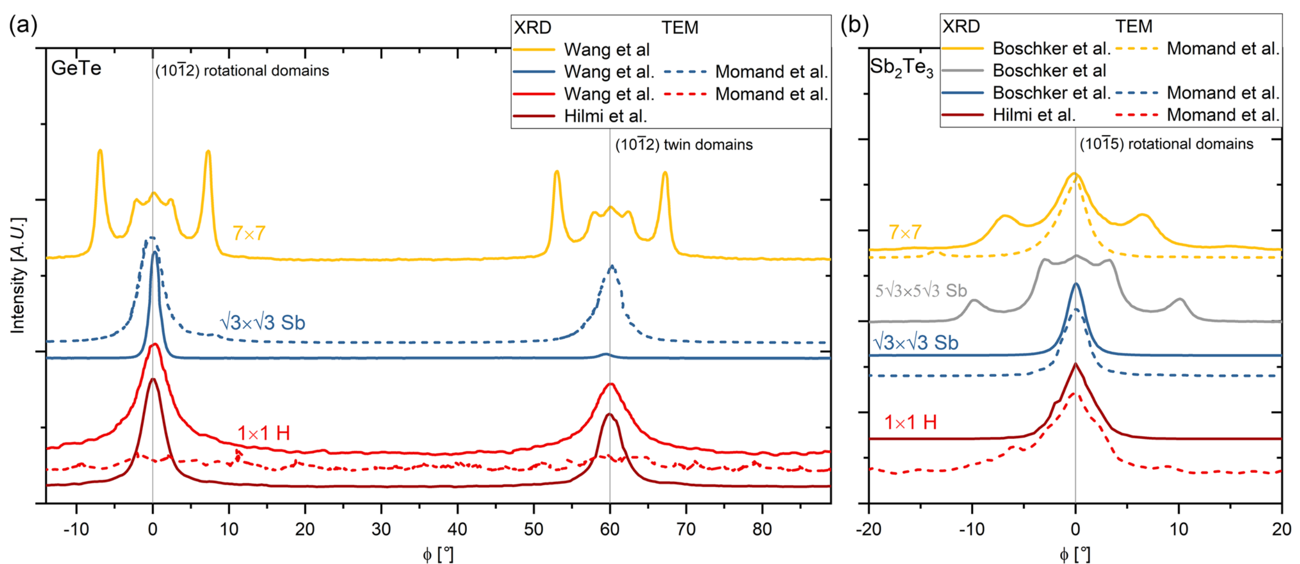

Figure 1. In-plane alignment scans of the $(10\bar{1}2)$ peak of GeTe a) and Sb_2Te_3 b) Closed lines represent Φ scans from XRD, while dashed lines are extracted from TEM experiments. The Φ angle is set in relation to the Silicon $(1\bar{1}0)$ orientation. The films grown on H passivated Silicon show the least degree of texture, and the films on $\sqrt{3} \times \sqrt{3}$ terminated Silicon the largest amount of texture. Suppression of the twin domain (at 60°) is reported for the Sb termination as well. Growth on the Si 7 × 7 and the $5\sqrt{3} \times 5\sqrt{3}$ domains show multiple rotational domains for each primary direction. Redrawn from refs. [21,22,24,35,37,48,49].

© 2024 The Authors. physica status solidi (a) applications and materials science published by Wiley-VCH GmbH

18626319, 2024, 22, Downloaded from https://onlinelibrary.wiley.com/doi/10.1002/pssa.202300921 by Forschungszentrum Jülich GmbH Research Center, Wiley Online Library on [21/11/2024]. See the Terms and Conditions (https://onlinelibrary.wiley.com/terms-and-conditions) on Wiley Online Library for rules of use; OA articles are governed by the applicable Creative Commons License

18626319, 2024, 22, Downloaded from https://onlinelibrary.wiley.com/doi/10.1002/pssa.202300921 by Forschungszentrum Jülich GmbH Research Center, Wiley Online Library on [21/11/2024]. See the Terms and Conditions (https://onlinelibrary.wiley.com/terms-and-conditions) on Wiley Online Library for rules of use; OA articles are governed by the applicable Creative Commons License

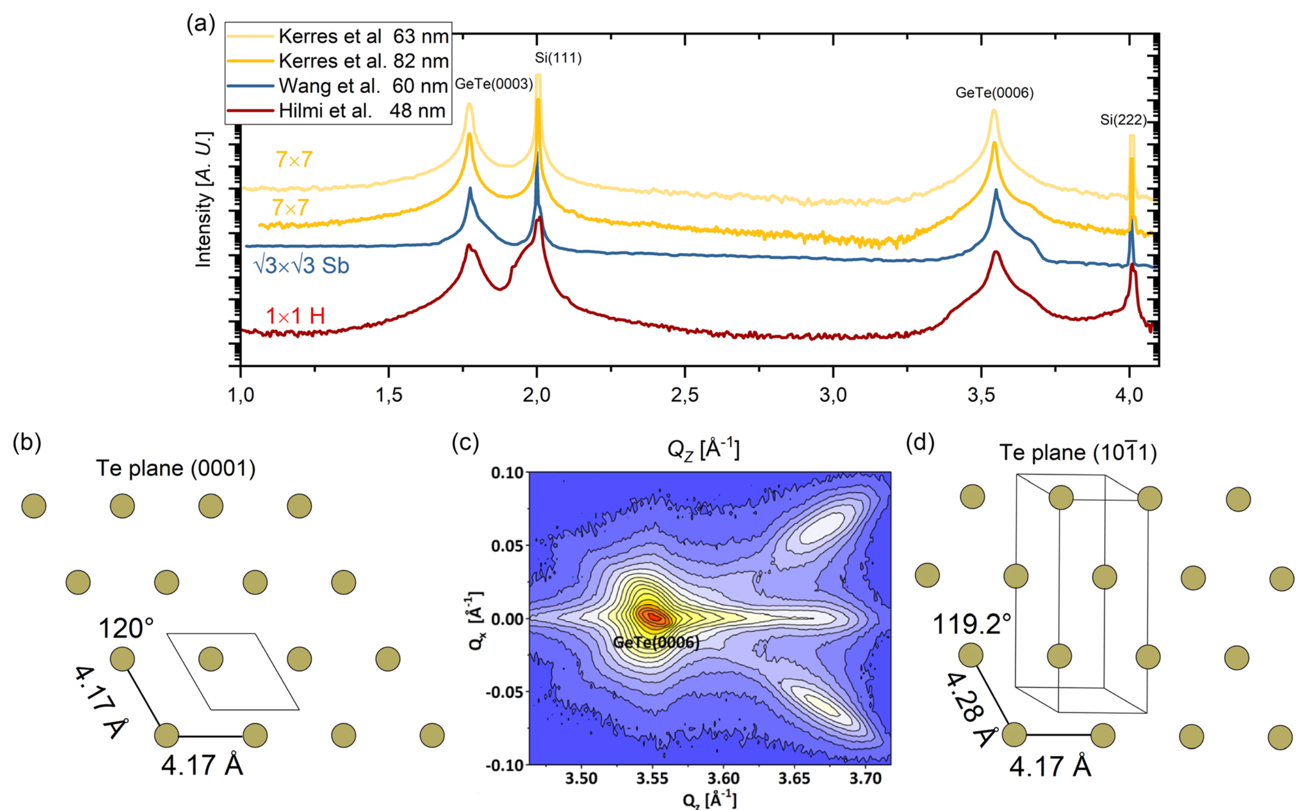

Figure 2. a) Θ 2Θ measurements of textured GeTe films on different Si terminations. Facets with (0001) direction are prevalent in the film. For all substrates, shoulders on the high angle side of the (0006) peak are visible, which can be suppressed for optimal growth e.g., on the 7 × 7 surface. Redrawn from refs. [22,37,51]. b) Top view of Te atoms on the (0001) plane, with the two planar lattice vectors equal to the a/b constants from the unit cell c) A reciprocal space map of the GeTe (0006) peak reveals that the shoulder contains three individual peaks from 3 rotational alignments of grains with (10$\bar{1}$1) orientation. The sketches on the left and right show the close similarity of the two crystal planes. d) Top view of the Te (10$\bar{1}$1) plane. Compared to the (0001) plane, one planar lattice vector is slightly elongated and their angle is slightly decreased. (c) is Reproduced with permission.[22] Copyright 2014 American Chemical Society.

materials, facets with a different out-of-plane orientation are suppressed for the substrates discussed here.

Concerning the three different surface terminations of Si(111) wafers discussed so far, the Sb/Bi termination seems to be the best choice for controlled thin film growth with only one rotational domain. However, it has drawbacks. Depositing the Sb monolayer requires a high-temperature step, which is incompatible with CMOS back end of line processes. Furthermore, the adatoms can diffuse into the substrate, doping it and making it too conductive for room temperature transport measurements. The 7 × 7 surface has a similar compatibility problem regarding temperature but remains highly insulating. Hence, electrical measurements on such samples can be performed without complications. Yet, the additional rotational domains might lead to an increased resistance for in-plane charge transport. However, for applications designed to work cross-plane, perpendicular to the layered structure (as utilized in the devices shown later), only the out-of-plane texture is important, i.e., a good fiber texture is satisfactory. The H passivated Si suffers from a lack of controllability due to a broad range of desorption temperatures, if HF is used together with rinsing in De ionized water. This problem can be circumvented if the etching method is shifted to a NH_4 wet etch, which can produce perfect H:Si surfaces that are stable up to 480 °C.[50] Nevertheless, the growth on such substrates so far is inferior compared to the other substrate modifications.

To gain further insight into the bonding of the thin films to the substrates, cross-section TEM images of films on different terminations are compared. In **Figure 3**, the interfaces between the Si substrate and Sb_2Te_3 (left side) as well as GeTe films (right side) are shown. All layers feature a bright (Sb or Te) layer directly above the Si surface. In the images of Sb_2Te_3, the gap at the interface is larger compared to the pseudo van der Waals gaps inside the film. Interestingly, the passivation layer and the increased gap spacing are present independent of the surface termination of Si(111). To further understand the initial growth of the films, the atomic species next to the substrate should be identified. In Sb_2Te_3 films, it is difficult to distinguish between the cation (Sb) and the anion (Te) due to their similarity in atomic number. In Bi_2Te_3 films however, the difference is larger, and the starting layer can be attributed to an initial Te monolayer right above the surface, which passivates it, under appropriate deposition conditions.[28] It has recently been shown that Sb atoms which have passivated the Si substrate diffuse into the growing film, causing the initial layer right above the Si substrate to switch

© 2024 The Authors. physica status solidi (a) applications and materials science published by Wiley-VCH GmbH

18626319, 2024, 22, Downloaded from https://onlinelibrary.wiley.com/doi/10.1002/pssa.202300921 by Forschungszentrum Jülich GmbH Research Center, Wiley Online Library on [21/11/2024]. See the Terms and Conditions (https://onlinelibrary.wiley.com/terms-and-conditions) on Wiley Online Library for rules of use; OA articles are governed by the applicable Creative Commons License

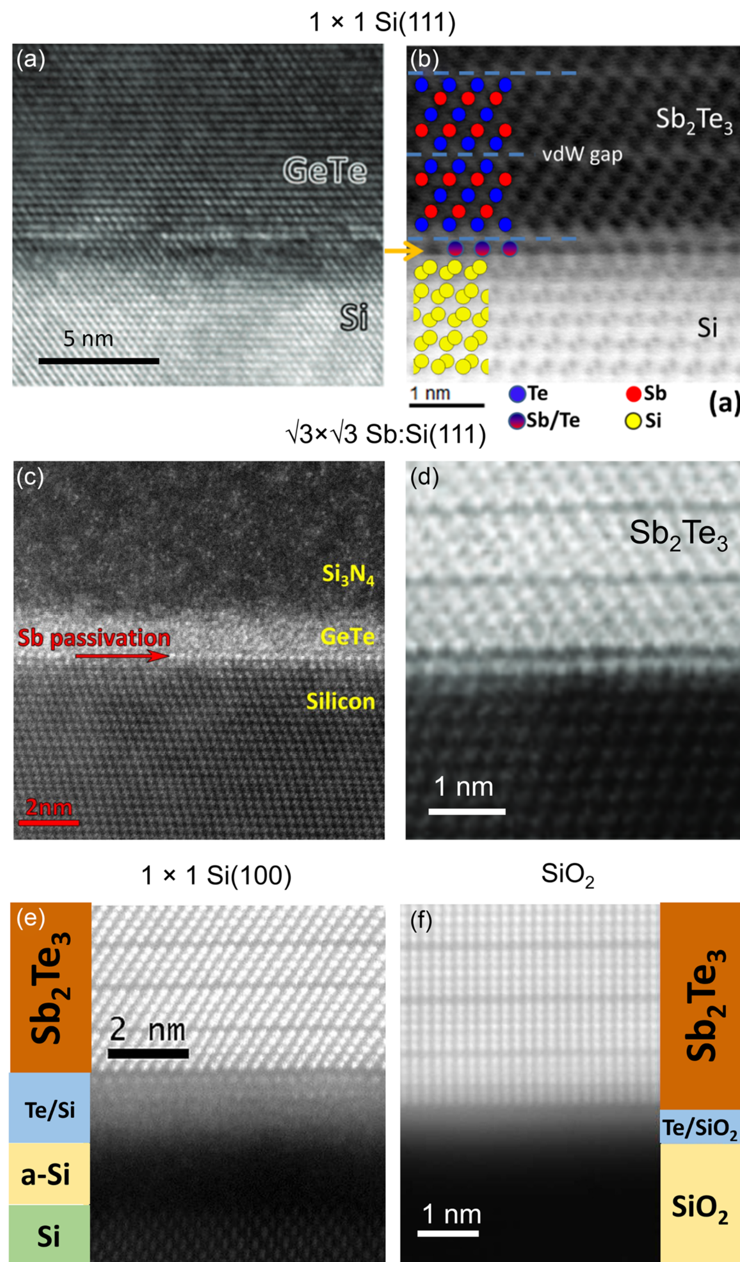

Figure 3. Cross section images of the interfaces between thin film and substrate obtained by HR-TEM.: a,c) GeTe on 1 × 1 Si(111) and $\sqrt{3} \times \sqrt{3}$ Si(111). A Sb/Te passivation layer is still present after the deposition on the Sb terminated Silicon. b,d) Sb_2Te_3 on on 1 × 1 Si(111) and $\sqrt{3} \times \sqrt{3}$ Si(111). A passivation layer is visible for both substrates after Sb_2Te_3 has been deposited. e,f) Sb_2Te_3 on Si(100) and SiO_2 substrates. If sputtered with Te excess from the start of growth, Sb_2Te_3 can grow textured even on amorphous Silicon(oxide) with a Te/SiOx intermixed region.[40] Reproduced under the terms of the CC BY 3.0 license.[48] Copyright 2017, The Authors. Published by Springer Nature, (b) Reproduced under the terms of the CC BY 3.0 license.[35] Copyright 2017, The Authors. Published by AIP Publishing (c) Reproduced under the terms of the CC BY 3.0 license.[91] Copyright 2016, The Authors. Published by Springer Nature (d) Reproduced with permission.[113] Copyright 2017, RCS Pub (e,f) Reproduced with permission.[40] Copyright 2020, IOP Publishing.

from Sb to Te.[34] The interfacial, passivating Te layer can also be formed on amorphous substrates under tellurium excess at the growth start.[40] This enables the growth of high-quality fiber-textured films for devices.

The formation conditions of a passivation layer seem to depend on the surface chemistry and morphology as well. Excess of Te at the growth start seems to be required for Te passivation of SiO_2, but not necessarily for the passivation of the Si(111) interface. In a similar experiment, Ross et al. showed that substoichiometric GST (5% loss in Te composition due to desorption, when GST films are deposited from stoichiometric targets at high temperatures) still forms a passivation layer on

© 2024 The Authors. physica status solidi (a) applications and materials science published by Wiley-VCH GmbH

18626319, 2024, 22, Downloaded from https://onlinelibrary.wiley.com/doi/10.1002/pssa.202300921 by Forschungszentrum Jülich GmbH Research Center, Wiley Online Library on [21/11/2024]. See the Terms and Conditions (https://onlinelibrary.wiley.com/terms-and-conditions) on Wiley Online Library for rules of use; OA articles are governed by the applicable Creative Commons License

Si(111). Yet, no textured growth could be achieved on SiO_2.[54] Momand et al have shown that on sputtered SiO_2, grains on smooth parts of the sample are aligned parallel to the surface, while randomly oriented grains form on rough parts.[18]

As the passivation layer seems to work similarly on textured and amorphous substrates, the question arises, how the Te atoms align on the Si surface. The Te-Si(111) surface was initially reported as a stable Te/Si(111) 1×1 surface reconstruction without changing the lattice parameter of the surface. Yet, the surface conductivity is fairly low considering the high density of states (DOS) presented in the accompanying density functional theory (DFT) calculations.[55] A finite temperature DFT molecular Dynamics simulation[56] subsequently proposed a model that consists of a locally disordered passivation layer, which averages to an observed 1×1 structure in low energy electron diffraction (LEED) experiments. This disordered layer forms a semiconductor with a narrow band gap of about 0.3 eV, which could explain the measured conductivity. While the surface arrangement of the passivation is still a topic for current research, especially for the amorphous substrates, it is nevertheless a novel and interesting approach to grow chalcogenides for application.

2.2. The Use of V2-VI3 Seed Layers & Textured Crystallization from Interfaces

The importance of the Te interfacial layer for the growth of textured chalcogenide films has only recently been found. Hence, attempts to grow monochalcogenides with the use of the Te termination are topics of ongoing research. However, attempts to use Sb_2Te_3 as a seed layer for subsequent growth of GeTe/GST have a longer history and will therefore be discussed here. Sb_2Te_3 is attractive as a seed layer due to its good biaxial alignment on suitable crystalline substrates as discussed above. Furthermore, the ability of Sb_2Te_3[57] (and GST compounds[58]) to form fiber-textured films on amorphous substrates, either during annealing & crystallization of ultrathin films, or directly during high-temperature growth is appealing. It can be seen in the EBSD images in **Figure 4**a,b, that GeTe films grown on Sb_2Te_3 seeds, adapt the texture of Sb_2Te_3.[9] Again, due to the similarity of the (0001) and $(01\bar{1}1)$ planes in GeTe, the area of grains not oriented around the (0001) direction is larger than for Sb_2Te_3. Yet, the in-plane alignment of the seeded films is sharper compared to GeTe directly grown on Si(111). On the Interface between Sb_2Te_3 and GeTe, a Te-gap-Te-Sb-Te-Ge... stacking is observed.[18] This stacking imprints the crystallographic direction from the quintuple into the GeTe film formed above. Besides preserving the epitaxial alignment, the Sb_2Te_3 seed also lowers the required growth temperature for epitaxial GeTe by ≈60 °C and modifies the growth mode to achieve a flat and coalescent layer growth, as shown in the SEM images of Figure 4c,d.[37]

Along with the crystallographic direction, also some stress due to lattice mismatch is imposed across the gap. This coupling is stronger than expected for 2D systems if only weak van der Waals forces are present across the gap. This coupling leads to strains in a growing superlattice which can be monitored by RHEED and modeled by a spring model,[36,59] with a coupling factor $0 \leq \varepsilon \leq 1$ across the gap. The model from Wang et al.[59] implies that depositing a material with a larger lattice constant on top of a material with a lower lattice constant will put tensile stress on the layer below, just as it will impose compressive stress on the newly deposited layer. The model of Vermeulen et al.[36] works on the premise that strain relaxation occurs through dislocation incorporation. He therefore also uses a model that employs a restoring force in the newly grown strained layer, but now with a damping term to model dislocation formation. Both models can account for the observed dependence of the strain in growing superlattices. On the contrary, this behavior cannot be explained based on true van der Waals bonds across the heterostructure. Due to the increased bond strength compared to 2D materials in the gaps of layered MVB chalcogenides, we instead refer to them as pseudo van der Waals gaps.

To study the restoring force, which preserves the epitaxial stacking of these layers, in detail, energy differences between stable chalcogenides and structures containing twins and translational shear faults have been calculated.[60] While 2D materials like GaSe have glide paths where shearing does not require significant energy cost, energy barriers between 10 and 60 meV A^{-2} stabilize the stacking of Sb_2Te_3 films. Hence, in TEM many more stacking faults are observed in true 2D materials like GaSe as compared with films of Sb_2Te_3 or GeTe/Sb_2Te_3 heterostructures. This difference has been attributed to MVB across the gap.[60] Due to the extended chains of p orbital formed in the Sb_2Te_3 quintuples,[4] a significant bonding contribution exists between these quintuples, which can be measured with several bond indicators.[61–63] Even for the twinned structure, a lower but still significant bonding contribution exists.[61] As a side note, transition metal dichalcogenides (TMDCs) such as WSe_2 are considered as the workhorse of 2D materials besides graphene and hexagonal boron nitride. They indeed are held together by weak van der Waals forces across the chalcogenide layers. Very recently it could be shown that a subgroup of these TMDCs including $PtTe_2$ also show some form of interlayer bonding besides van der Waals interaction[64] However, further extensive studies on the interlayer bonding of TMDCs are missing to our knowledge.

The improved structural quality of GeTe films grown on an Sb_2Te_3 template can even be seen if an amorphous film has been deposited initially. Being able to start crystallization from the interface, GeTe crystals grow biaxially textured on the Sb_2Te_3 seed layer at temperatures 95 °C lower than for crystallization without a template.[13] This improved texture also leads to a much larger change in the optical properties between the amorphous state and the crystalline phase, as the crystalline state is much closer to a perfect single crystalline phase.[13]

In the following, high-temperature growth on Sb_2Te_3 seed layers is compared to two step growth procedures, where a layer deposited at room temperature is annealed subsequently. This two-step process has been shown to increase both vertical and lateral grain sizes of the resulting film (Figure 6a,b), if a seed layer with a sufficiently smooth surface can be grown.[57] For sputter deposition on Si(100) at room temperature and subsequent crystallization, root means squared (RMS) roughnesses as low as 2 Å are reported for 3 nm films, with increased roughnesses for both thinner and thicker films. A similar trend of an "optimal" thickness can also be seen in high-temperature grown MBE films on Si (111), both by an increase in the maximum

© 2024 The Authors. physica status solidi (a) applications and materials science published by Wiley-VCH GmbH

18626319, 2024, 22, Downloaded from https://onlinelibrary.wiley.com/doi/10.1002/pssa.202300921 by Forschungszentrum Jülich GmbH Research Center, Wiley Online Library on [21/11/2024]. See the Terms and Conditions (https://onlinelibrary.wiley.com/terms-and-conditions) on Wiley Online Library for rules of use; OA articles are governed by the applicable Creative Commons License

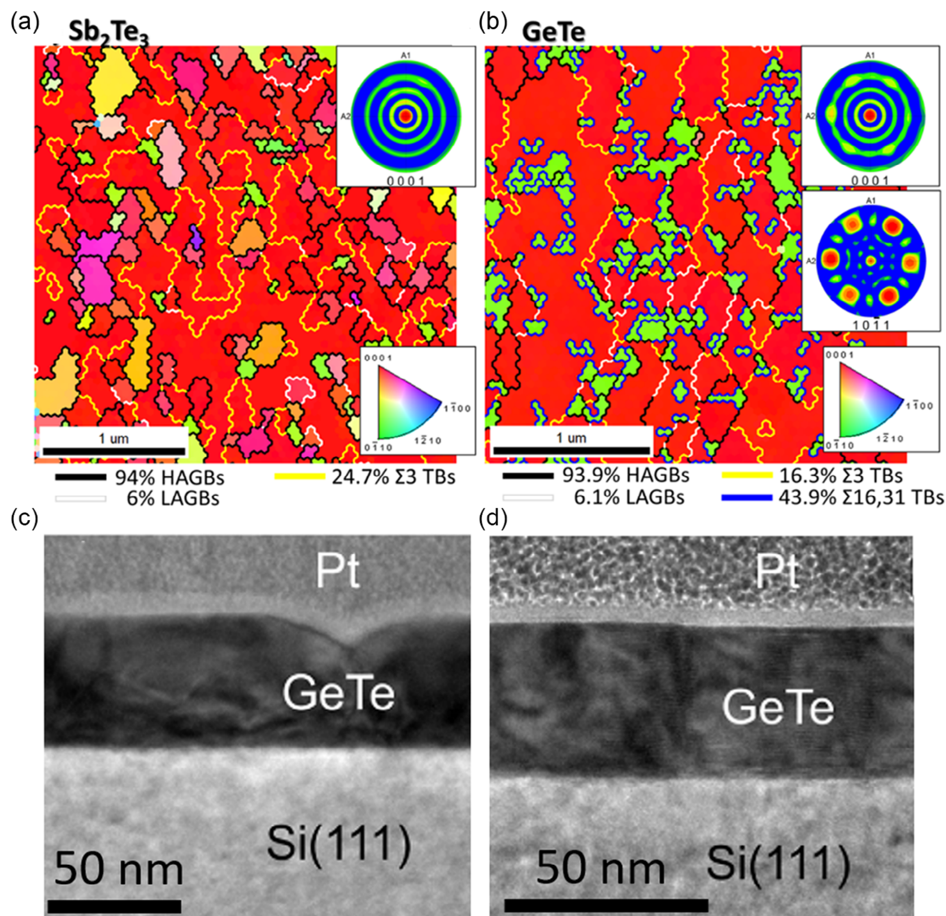

Figure 4. a,b) Comparison of the inverse pole figure map obtained from Electron Backscatter Diffraction (EBSD) on Sb_2Te_3 and GeTe on an Sb_2Te_3 seed. Te insets show the texture analysis along the (0001) and (10$\bar{1}$1) pole. GeTe grown on the seed layer adapts the out-of-plane and in-plane orientation of Sb_2Te_3. Reproduced with permission.[9] Copyright 2019, IOP Publishing. c,d) Cross section SEM of GeTe grown without seed (top) and with seed (bottom). Using a seed layer, the GeTe growth mode changes to flat coalescent growth instead of large islands. Reproduced with permission.[37] Copyright 2019, Elsevier.

RHEED intensities, and evaluation of X-ray reflectivity measurements.[63]

As both processes show similar trends, it is worthwhile to explore the differences between them. A study of growth and texture of room temperature, annealed and high-temperature Sb_2Te_3 films grown with MOCVD was performed for both Si(100)[65] and Si(111)[66] surfaces as presented in **Figure 5**.

On both surfaces, post growth annealing (cf. Figure 5b,e) leads to a higher degree of texture and larger grains of the Sb_2Te_3 layer. Comparing the in-plane alignment, Sb_2Te_3 on Si(100) performed worse than on Si(111). The twist per rotational domain is larger, and due to the differences in the three-fold symmetry of Sb_2Te_3 compared to the four-fold symmetry of the (100) surface, one rotational domain can be found at each 90° rotation, resulting in 12 peaks.

In addition, the growth of Sb_2Te_3 on amorphous substrates such as SiO_2 and a-Al_2O_3 has been studied. Post growth annealing leads in all cases to the best texture and smoothness of the film, while high-temperature deposition on SiO_2 even resulted in island growth. This raises the question, for which materials and substrates the two-step process can be beneficial. Regarding materials, a large enough anisotropy, or to rephrase this, the presence of Te–Te van der Waals like bonds in the crystal structure seems to be important. The increased order in post-annealed films can be extended to GST compounds. On Si(111) substrates, post-annealing is shown to produce high-quality trigonal GST films, whether from an amorphous start[60] or the disordered cubic phase.[53] Such behavior has not been reported for GeTe, to our knowledge. Instead, GeTe is prone to form trans-rotational crystals upon crystallization,[49] which leads to a lowering of in-plane alignment, even if a single crystalline surface is used. Recently it has also been shown that Sb films can be grown with a high degree of texture with a similar 2-step method,[67] albeit only on amorphous substrates. The feasibility of this approach for single crystalline surfaces has to our knowledge yet to be investigated.

A small outlook shall be given to the search for other possible substrates for epitaxial growth besides Si. One prevalent idea for the behavior of different substrates is to look for materials with chemical selectivity,[68] i.e., materials that only form compounds

© 2024 The Authors. physica status solidi (a) applications and materials science published by Wiley-VCH GmbH

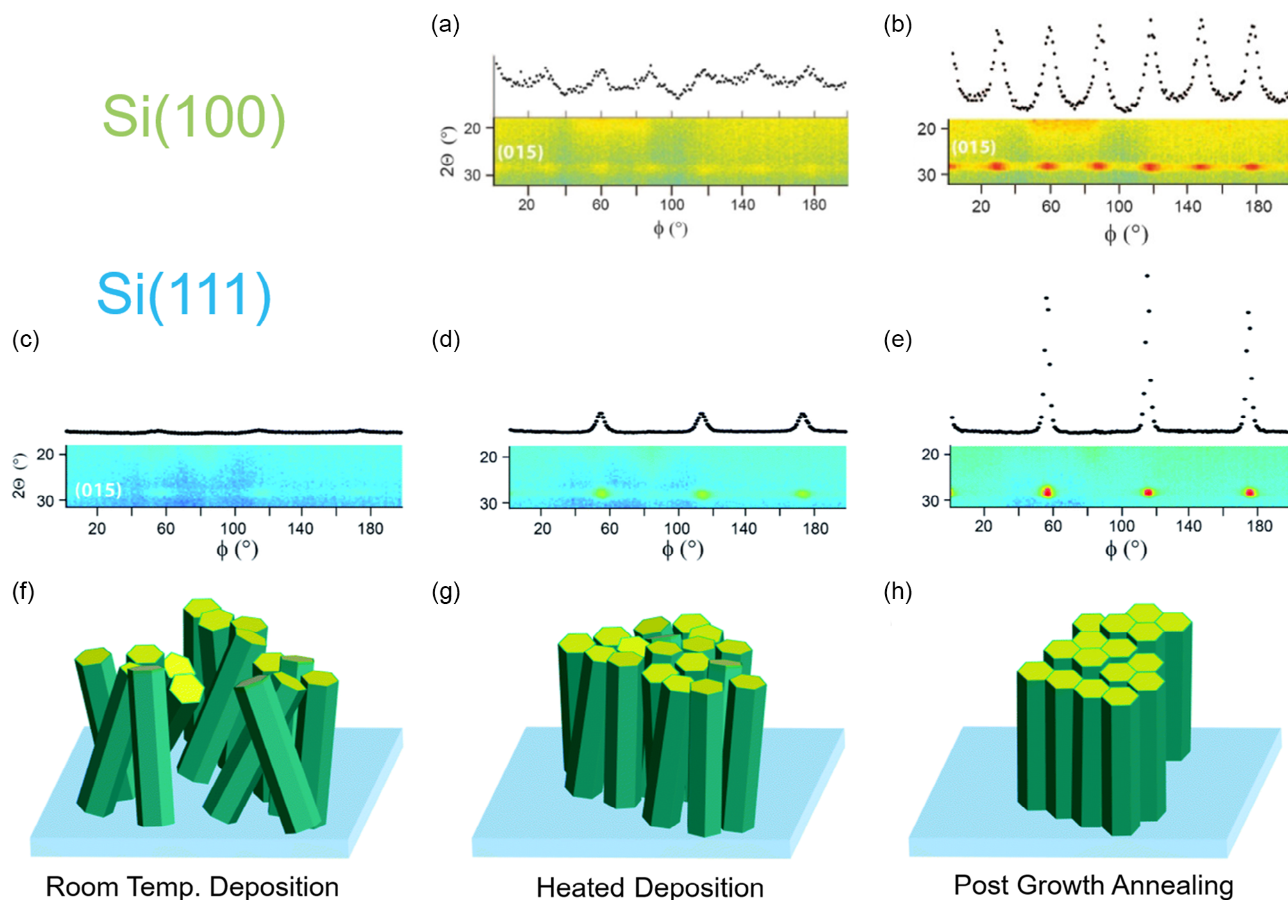

Figure 5. Comparison of the texture of Sb_2Te_3 grown on Si (111) and Si (100) for three different deposition conditions. a–e) show reciprocal space maps of the (015) peak, with Φ on the *x* axis and 2Θ on the *y* axis. Results for heated deposition and Post growth annealing Si(100) are shown in (a) and (b) in this order. Results on Si(111) for Room temperature, heated deposition and post growth Annealing are shown in (c–e) in this order. f–h) show sketches of the texture obtained from each deposition method. The twist of the crystallites, causing the peak broadening in Φ is lower for the Si(111) surface. Furthermore, post growth annealing drastically increases the peak height, which can be attributed to a lowering of the tilt of the crystallites as well. (a,b) Reproduced under the terms of the CC BY 3.0 license.[65] Copyright 2021, The Authors. Published by American Chemical Society. (c–h) Reproduced with permission.[66] Copyright 2020, RSC Publishing.

or solids solutions with either Sb or Te. This suggests a list of six possible elements (Si, P, Ge, W, Re, and Pb). From this list, fiber-textured growth has been reported experimentally on Si and W, with a Te layer passivating the surface. Oxide surfaces, however, show no selectivity due to the ease of the formation of Sb and Te oxides. Thin films on SiOx are thus randomly oriented. Just following the selectivity argument, Al_2O_3 films would be equally bad substrates. However, films growing on Al_2O_3 show a good amount of texture, despite the presence of oxygen. This can be explained if the formation enthalpy of all oxides in question is considered, besides the general statement that such an oxide exists. For SiO_2, the standard formation enthalpy $\Delta_f H_m°$ is $-910.86\,kJ\,mol^{-1}$,[69] still close to the standard formation enthalpy of Sb_2O_3 ($-710\,kJ\,mol^{-1}$),[70] while TeO_2 is with $-320\,kJ\,mol^{-1}$[71] the least stable compound. The standard formation enthalpy of Al_2O_3 is $-1675\,kJ\,mol^{-1}$[72] and thus much lower compared to that of Sb_2O_3. Consequentially, the Al_2O_3 surface is sufficiently passivated. In addition, amorphous carbon,[20] graphene[26] or Muscovite MICA (SiAlOx layer at the surface) serve as substrates for the growth of textured chalcogenide films.[41] Therefore, either surfaces with a preferential bonding to Te, a sufficient smoothness and/or passivation facilitate growth in a preferential direction. For example, SiOx surfaces can be used to grow fiber-textured films after a pretreatment with ion bombardment or E-beam.[20]

The exact mechanism why and under which conditions a passivating Te monolayer self assembles during crystallization/growth is still an open question. Yet, a practical solution to improve film growth is providing elemental Te a few seconds before the actual growth starts, to form a Te excess at the surface[28,40] before the film growth starts. The excess Te that is not needed for the formation of the surface passivation will either incorporate into the film to minimize Te vacancies or be reevaporated if the growth temperature is high enough.

This concludes the film growth aspect of the review, and the next part will deal with recrystallization experiments in textured films. We will answer the question whether the texture and crystal structure will be recovered in the recrystallized spots and

© 2024 The Authors. physica status solidi (a) applications and materials science published by Wiley-VCH GmbH

18626319, 2024, 22, Downloaded from https://onlinelibrary.wiley.com/doi/10.1002/pssa.202300921 by Forschungszentrum Jülich GmbH Research Center, Wiley Online Library on [21/11/2024]. See the Terms and Conditions (https://onlinelibrary.wiley.com/terms-and-conditions) on Wiley Online Library for rules of use; OA articles are governed by the applicable Creative Commons License

18626319, 2024, 22, Downloaded from https://onlinelibrary.wiley.com/doi/10.1002/pssa.202300921 by Forschungszentrum Jülich GmbH Research Center, Wiley Online Library on [21/11/2024]. See the Terms and Conditions (https://onlinelibrary.wiley.com/terms-and-conditions) on Wiley Online Library for rules of use; OA articles are governed by the applicable Creative Commons License

whether the crystallization speed is affected by the textured matrix.

2.3. (Re)crystallization

As mentioned earlier, directly providing a template for crystallization enables crystal growth once a sufficient crystallization temperature is reached. This template ideally makes nucleation obsolete since the film can grow crystalline directly from the interface. Collecting recrystallization data on textured GST compounds at low and high temperatures is reported in two different experiments, local amorphization due to ion implantation and subsequent crystallization in a TEM[14]and by melting upon laser excitation.[39,73] These two experiments will be summarized in the following.

Figure 6a–c show a TEM study of recrystallization at low temperatures. A highly textured GST deposited by MBE is bombarded by ions creating an array of amorphous dots with diameters of 50 and 100 nm. Inside the dots both GST and the underlying Si(111) surface are amorphized. At 90 °C, a crystalline annulus could be seen moving inwards at low velocities (2.6 pm s^{-1}). At 110 °C, recrystallization occurs purely from the sidewalls of the spots. The regrowth proceeds epitaxially with a high crystal growth velocity of around 170 pm s^{-1}.[14]

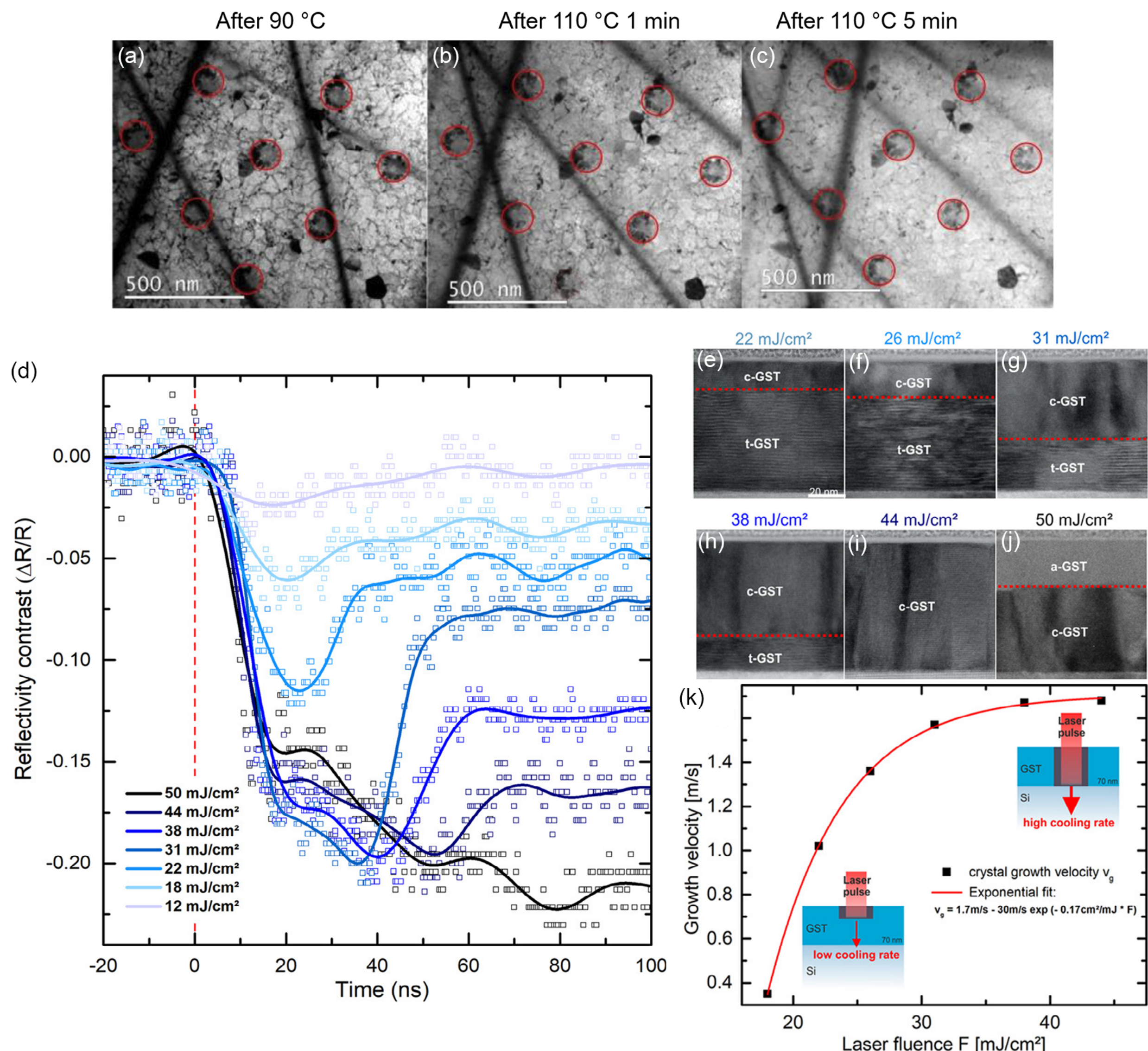

Figure 6. Recrystallization experiments of GST at low and high temperatures. a–c) TEM images of amorphized spots inside an epitaxially grown film. Upon Isothermal annealing the spots disappear as the film crystallizes. d) Transient reflectivity curves of lader irradiated textured GST films at different fluences show the time between melting (drop in intensity) and full recrystallization (recovery of the intensity plateau). A decrease in the reflectivity of the final state is due to the formation of cubic GST instead of trigonal GST e–j).cross section STEM images of the switched areas show the crystallization depth. At 44 mJ cm^{-2}, the film is molten up to the interface and at 50 mJ cm^{-2} an amorphous region remains at the top. The resulting growth velocities are shown in (e). (a–c) Reproduced with permission.[14] Copyright 2020, IOP Publishing. d–k) Reproduced with permission.[39] Copyright 2019, American Chemical Society.

© 2024 The Authors. physica status solidi (a) applications and materials science published by Wiley-VCH GmbH

18626319, 2024, 22, Downloaded from https://onlinelibrary.wiley.com/doi/10.1002/pssa.202300921 by Forschungszentrum Jülich GmbH Research Center, Wiley Online Library on [21/11/2024]. See the Terms and Conditions (https://onlinelibrary.wiley.com/terms-and-conditions) on Wiley Online Library for rules of use; OA articles are governed by the applicable Creative Commons License

Crystallization at high temperatures can be observed for instance in transient reflectivity measurements after laser irradiation of PLD grown GST shown in Figure 6d–k. The transient reflectivity (Figure 6d) is measured on the ns time scale after laser irradiation with varied fluence. With such laser pulses of a fixed length of 20 ns a trigonal epitaxial GST225 sample is irradiated. The fluence of the laser effectively determines the thickness of the molten region. This thickness can also be measured afterwards by the depth of the interface between the trigonal GST and the recrystallized cubic GST,[73] i.e., by cross section TEM images (Figure 6e–j) From the determination of the position of this interface, the crystal growth velocity can be determined (Figure 6k). The measured crystal growth velocities of up to 1.5 m s^{-1} are in line with the high-temperature crystal

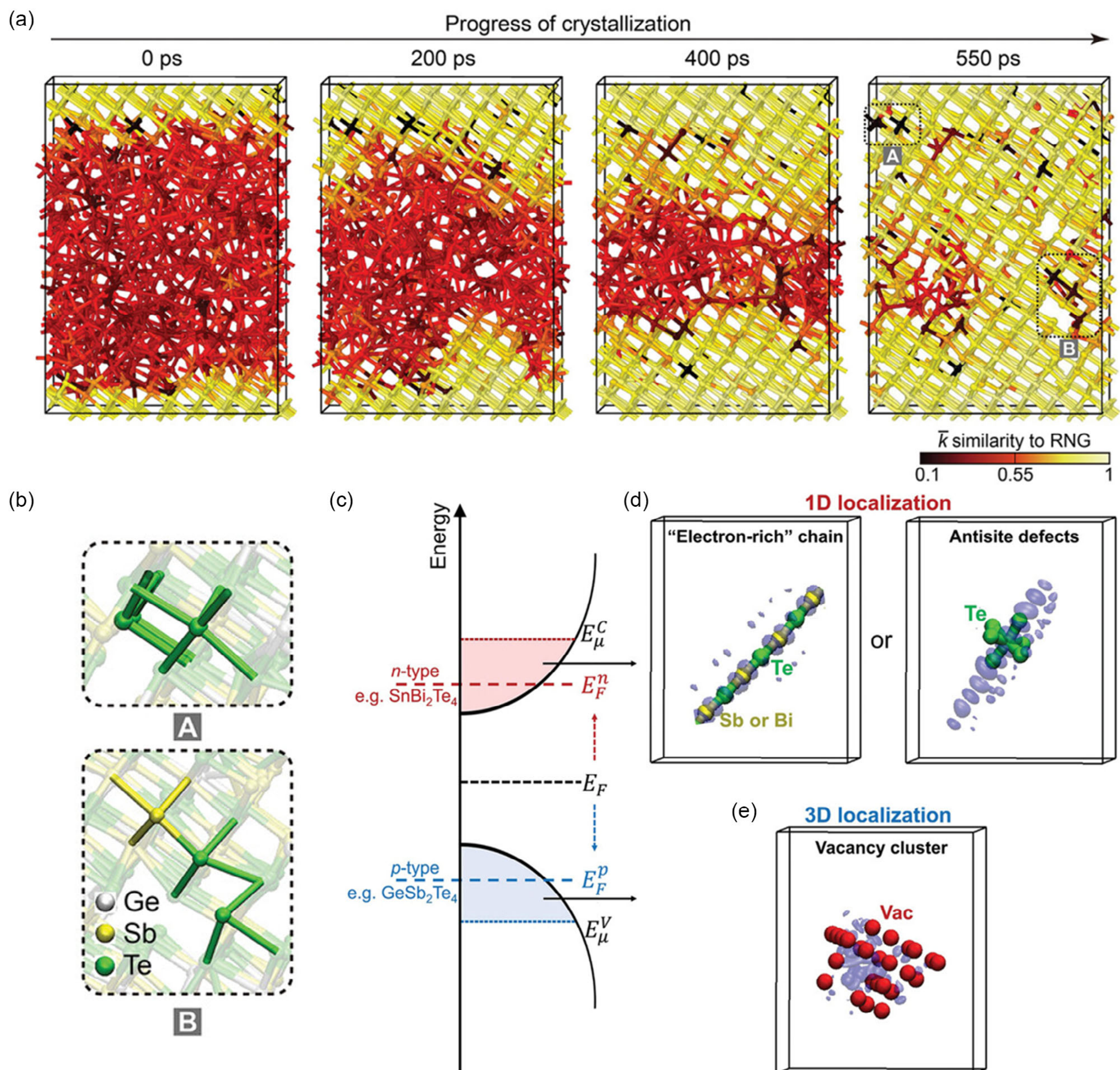

Figure 7. Large scale AIMD Simulation of the growth of GST124 from two crystalline interfaces. a) structure of the simulated volume. In the $\bar{k}$-similarity color scale, the yellow areas are crystalline and defect free. Crystallization occurs equally from both interfaces, recovering a single crystalline area afterwards. Dark areas in the crystalline matrix can be identified as defects, for example, the two areas containing antisite defects magnified in b). c) sketch of the band structure, highlighting the areas where localiziation can occur in the conduction and valence band. d) Isosurface of localized states in the conduction band, either around "electron rich" Sb–Te chains or Te antisite defects, both forming 1D localization lines. e) Isorfurface of localized states in the clocalized states in the valence band, appearing at vacancy clusters. Reproduced under the terms of the CC BY 3.0 license.[75] Copyright 2022, The Authors. Published by Wiley-VCH GmbH.

growth velocities obtained by Ab initio molecular dynamics (AIMD) Simulations for GST225(1.5 m s^{-1} at 700 K)[74] and GST124(1.5 m s^{-1} at 630 K).[75]

Apart from corroborating the results obtained from the experiments, the large-scale simulations have one important advantage. While high-angle angular dark-feld (HAADF) TEM images are able to distinguish between Ge and Sb/Te due to the larger difference in the atomic number, Sb and Te are harder to differentiate. Thus, obtaining a reasonable result for the concentration of antisite defects or vacancies inside the ordered structure is nearly impossible. This problem does not exist for the atomistic simulations. The large-scale recrystallization study is able to reveal a number of previously unnoticed defect states in the crystal (**Figure 7**), which have an effect on the localization of charge carriers inside the film. With new advances in the field of machine-learned potentials for MD simulations, the system size can even be extended much further, enabling studies of the effect of grain boundaries and polycrystalline materials.[76]

3. Confinement Effects in Ultrathin Chalcogenides

With the established growth methods from the previous part, the growth of sufficiently well-textured ultrathin films is possible and

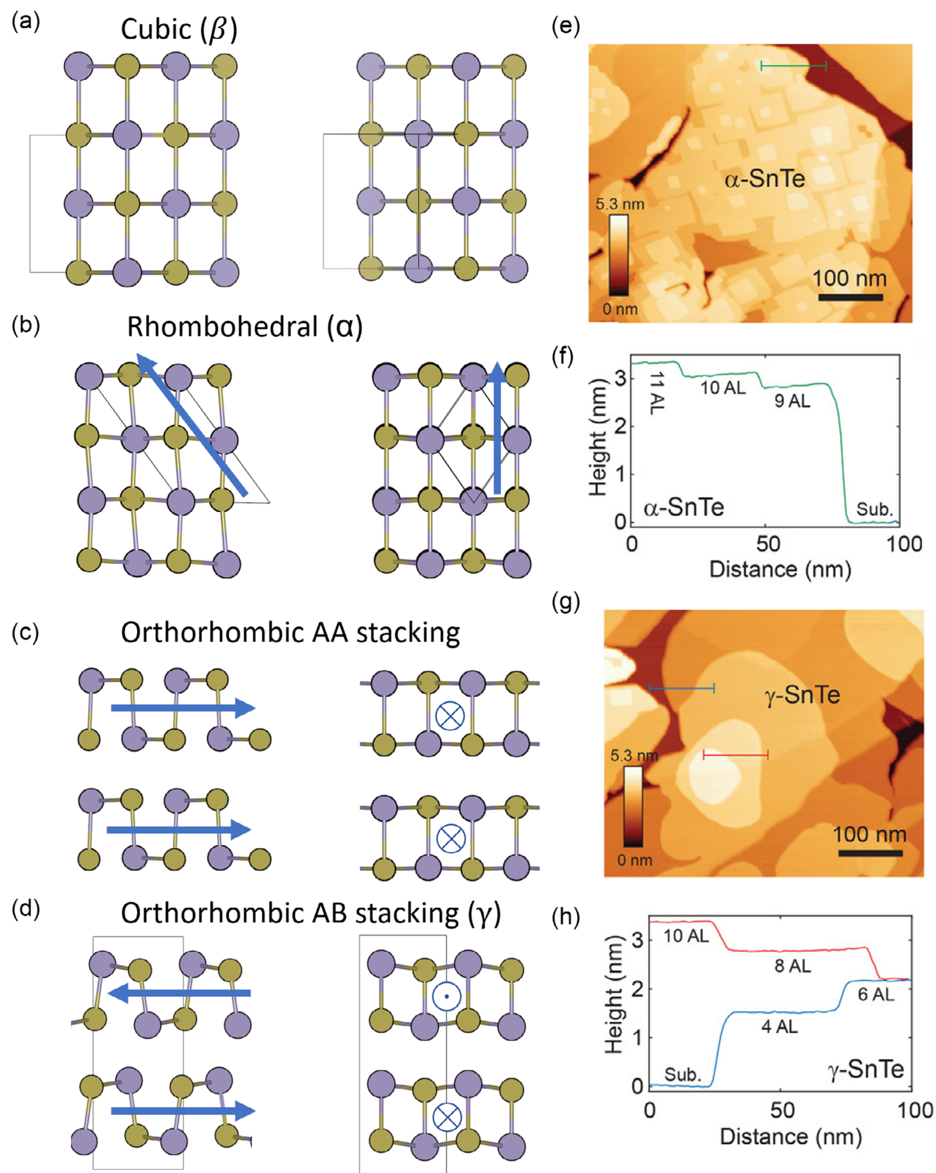

Figure 8. a–d) Side views of the cubic, rhombohedral and two possible orthorhombic stackings of SnTe. The rhombohedral unit cell features a Peierls distortion along the (111) direction, resulting in a net polarization along this directions. In the orthorhombic distortions, the net polarization of each bilayer occurs only in-plane in the cubic (110) direction. e–h) STM images and profiles of α- and γ- SnTe oriented in (100) obtained at 77 K. The rhombohedral stacking grows with atomic layer steps, while orthorhombic SnTe grows with steps of SnTe bilayers. Reproduced with permission.[81] Copyright 2018, Wiley-VCH GmbH.

© 2024 The Authors. physica status solidi (a) applications and materials science published by Wiley-VCH GmbH

18626319, 2024, 22, Downloaded from https://onlinelibrary.wiley.com/doi/10.1002/pssa.202300921 by Forschungszentrum Jülich GmbH Research Center, Wiley Online Library on [21/11/2024]. See the Terms and Conditions (https://onlinelibrary.wiley.com/terms-and-conditions) on Wiley Online Library for rules of use; OA articles are governed by the applicable Creative Commons License

18626319, 2024, 22, Downloaded from https://onlinelibrary.wiley.com/doi/10.1002/pssa.202300921 by Forschungszentrum Jülich GmbH Research Center, Wiley Online Library on [21/11/2024]. See the Terms and Conditions (https://onlinelibrary.wiley.com/terms-and-conditions) on Wiley Online Library for rules of use; OA articles are governed by the applicable Creative Commons License

corresponding results will be presented later in this chapter. In addition, the limitation to ultrathin films also enables comparative theoretical studies of free-standing slab models, even without the use of neural network potentials to study changes in both structure and bonding parameters upon confinement. As mentioned before, MVB chalcogenides form chains of highly directional p orbitals. These chains enable delocalization of electrons and metallic like behavior.[4] Therefore, this class of materials has also been called 'incipient metals'.[5] Depending on the angles between the atoms in the chain and the bond lengths in between, the degree of orbital overlap and therefore delocalization changes. The high symmetry case of the structures is characterized by equal bond lengths and an angle of 180° between the three atoms along the chain. Since such *p*-orbitals point in three orthogonal directions, an octahedral arrangement of atoms results. Any change from this high symmetry state will result in a lowering of the orbital overlap and an increase in the number of electrons localized between the two atoms with a shorter bond. This is also denoted as a Peierls distortion (PD) in analogy to the instability of a 1D chain of atoms.[77] In the three-dimensional case of chalcogenides, the buckling (changes in the angle) is happening simultaneously to the tendency of forming bilayers (n-tuples) with shorter and longer bonds.[78] Thus, the term "Peierls distortion" in chalcogenides refers to both changes. The bond length distribution is sufficient as an order parameter in these materials, as the bond angle distribution is intrinsically connected to it in this class of materials.

3.1. Changes in Structure and Bonding

This raises the question, how these materials react, when confined to the nanoscale. For this review, we focus on confinement in ultrathin films, with thicknesses in the range of 10 nm and below. It is clear, that for ultrathin films regardless of the material, the roles of surfaces and interfaces become more important. Yet, what happens if the bonding in the vicinity of the surface is governed by MVB formed by chains of overlapping p orbitals? It was already shown in the first part that lattice-matching interfaces of chalcogenides show a long-ranging influence, the effect of the interface visible even 10 nm above.[36] Confining these materials should lead to similar changes even far from the surface, as the atomic arrangement in the film adapts to the energetically favorable state. Along with the changes in atomic arrangement, changes in the optical and vibrational properties of the thin films are also expected. Such changes should also be very relevant for applications. Finally, the long range of the *p*–*p* orbital chains

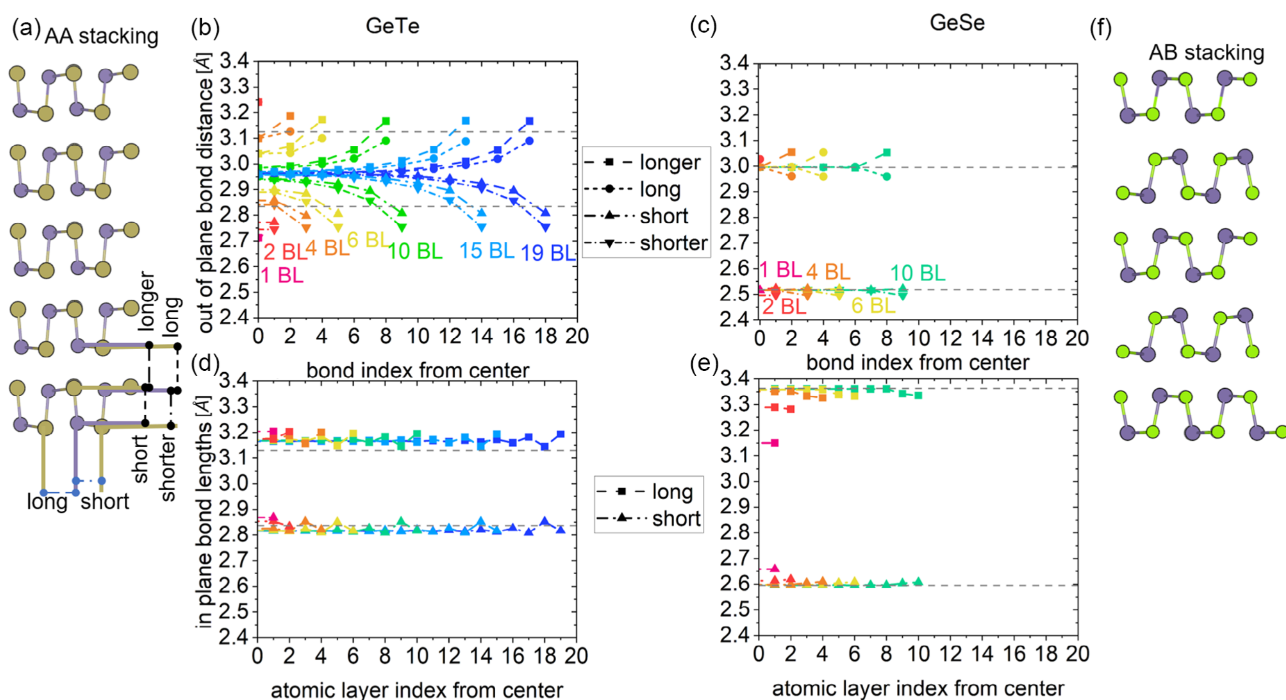

Figure 9. Structure of freestanding GeTe and GeSe thin film slabs with [100] orientation.[84] Outer sides: a,f) 2D projection of the corresponding unit cell. Both GeTe and GeSe show a bilayer stacking as an ultrathin film. While GeTe is still in an AA stacking, which resembles the stacking of the bulk structure, GeSe shows the expected AB stacking of the Pnma phase. b,c): bond distances along the out-of-plane direction for different slab thicknesses. The grey lines represent the distances in the bulk phase. The bond index is shown from the center to the edge. At the edges of the GeTe film (left) buckling occurs and two bond distances can be found in/between the bilayers. The buckling and pairing of bilayers gradually decrease toward the center, so that for film thicknesses above 10 bilayers, equal bond distances, and a cubic-like stacking are reached. For GeSe (right), buckling only occurs at the outermost layer and no changes in out-of-plane direction are visible. d,e) In-plane bond lengths for the stacks. The grey lines represent the bond lengths in the bulk phase GeTe showing the buckling effect in the short/long bonds as well for the in-plane bond lengths. However, the in-plane distortion does not vanish in the center of the slabs, but is larger than in the bulk structure. GeSe shows almost no effect of the buckling on the in-plane distortion, but a visible change toward the less distorted Cmcm phase for a thickness below four bilayers. Data points redrawn from ref. [84].

© 2024 The Authors. physica status solidi (a) applications and materials science published by Wiley-VCH GmbH

should even have interesting implications for the topologically protected surface states of MVB V_2–VI_3 compounds. The first material we want to focus on is SnTe. Confining this material to small dimensions can even lead to changes in the symmetry and phase of the crystal. At 0 K, SnTe is stable in a rhombohedral, "Peierls distorted" structure, similar to the room temperature structure of GeTe, albeit with smaller distortion. Consequently, this distortion can be overcome by thermal energy at lower temperatures compared to GeTe. Thus, the transition temperature between rhombohedral and cubic SnTe is between 50 and 100 K, depending on the carrier concentration.[79] A similar phase transition in GeTe can only be found at temperatures around 700 K.[80] However, in ultrathin films, the energy gain through delocalization is less feasible, and three additional phases can appear. The rhombohedral α phase with a PD in the (111) direction and two orthorhombic structures, which differ by the bilayer stacking sequence. In the γ-phase, every 2nd bilayer plane is mirrored, so that an AB stacking with alternating polarity is achieved. But also an AA stacking of Bilayers is feasible.[81–83] Sketches of the structures are shown in **Figure** 8a–d. Experimentally, only the α and γ phases have been reported, although, most of the phase identifications in ultrathin SnTe films have been based on scanning tunneling microscopy (STM) evaluations of the polar ordering (the rhombohedral structure is always polar) and step height (bilayer steps form for orthorhombic SnTe, while single layer steps form for rhombohedral SnTe). The differences between rhombohedral and orthorhombic SnTe morphologies are shown in Figure 8e–h.

For the theoretical investigation of structure, bonding and properties of ultrathin films besides SnTe, DFT calculations on (100) oriented slabs of rhombohedral GeTe and SnTe (both metavalent) and orthorhombic GeSe and SnSe (both covalent) have been performed.[84]

The structural fingerprints of selected GeTe and GeSe slabs are shown in **Figure 9**. GeSe (and SnSe) are stable in the orthorhombic AB stacking, which is expected from their bulk phase.

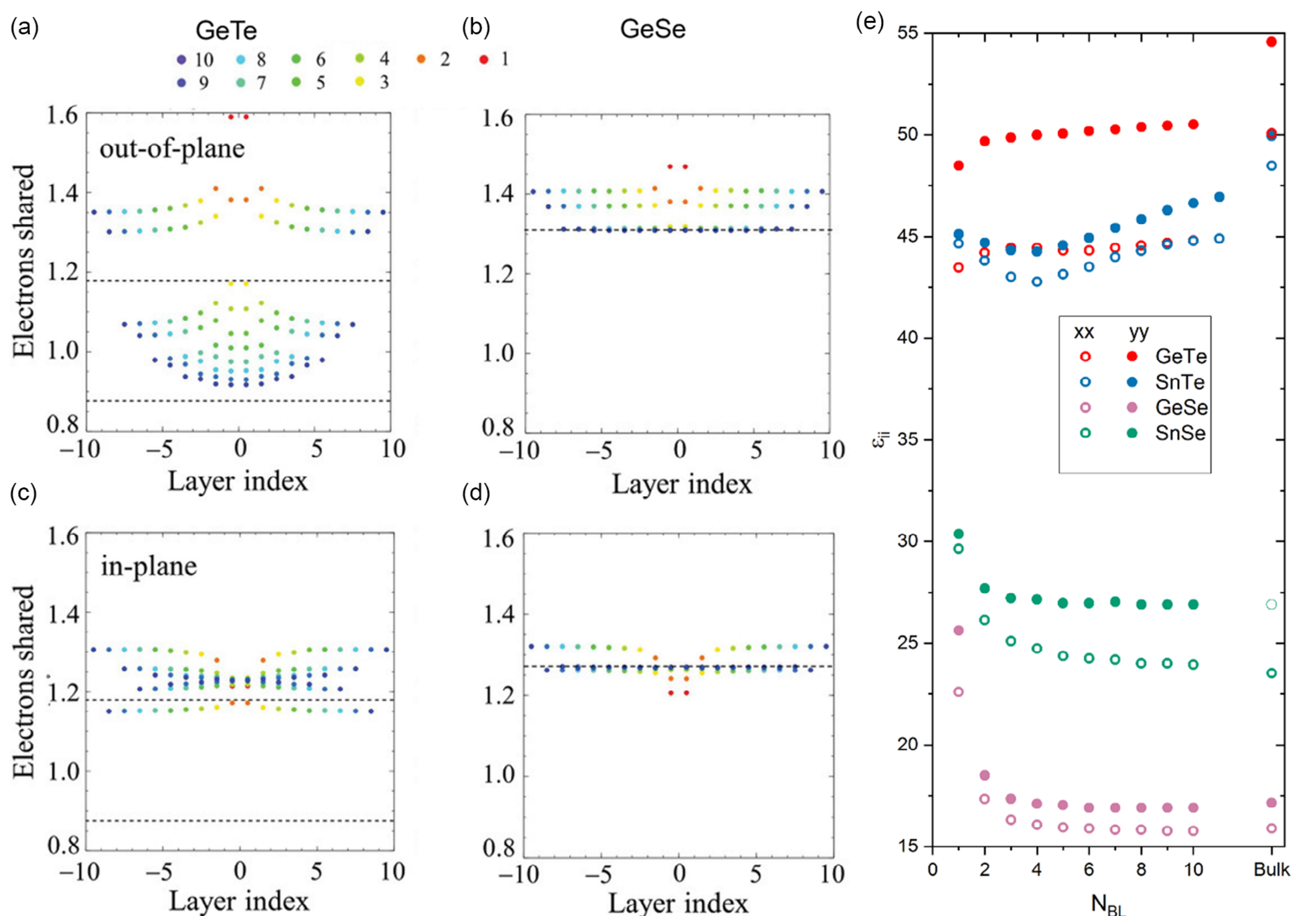

Figure 10. Bonding indicators and property changes in ultrathin chalcogenide slabs. a,b) Layer dependent number of electrons shared (ES) in out-of-plane direction for GeTe and GeSe, respectively. GeTe shows gradual changes in ES with the layer index and an overall trend toward higher ES for thinner films. For GeSe, the ES values remain constant for films thicker than 4 bilayers. c,d) The corresponding in-plane ES. For the ultrathin films, the in-plane ES value of GeSe drops below the bulk value. e) In-plane components of the static dielectric (permittivity) tensor for GeTe, SnTe, GeSe and SnSe. GeTe and SnTe show an increased distortion compared to the bulk and therefore lower values of the static permittivity. GeSe and SnSe show similar distortions in the thicker slabs as for bulk material and therefor similar ϵ values. The ultrathin GeSe and SnSe films are less distorted, which results in an increased ε; (a–d) Reproduced with permission.[84] Copyright 2020, Wiley-VCH GmbH. (e) redrawn from ref. [84].

© 2024 The Authors. physica status solidi (a) applications and materials science published by Wiley-VCH GmbH

18626319, 2024, 22, Downloaded from https://onlinelibrary.wiley.com/doi/10.1002/pssa.202300921 by Forschungszentrum Jülich GmbH Research Center, Wiley Online Library on [21/11/2024]. See the Terms and Conditions (https://onlinelibrary.wiley.com/terms-and-conditions) on Wiley Online Library for rules of use; OA articles are governed by the applicable Creative Commons License

GeTe (and SnTe) are however relaxed to a different phase than the bulk counterpart. As discussed before, the orthorhombic AA Bilayer stacking is obtained for thin films of both materials. Projections of the 5-layer slabs of GeTe and GeSe are shown in Figure 9a,e. For the out-of-plane bond distances and in-plane bond lengths in Figure 9b–d, the values of each bond in the slab are plotted with respect to its index from the slab center. Since both surfaces are identical, the slab geometry is symmetric and only one half is shown in the images. On the surface of the slabs, buckling occurs for all materials. Here the cations and anions shift away from the average z-position of the layer. Changes in the buckling for the surface and subsurface atomic layers result in a further split of the short and long bonds into four different out-of-plane bond distances. The in-plane bond lengths are not split. For the covalent material GeSe, the split vanishes after the first bilayer and bulk-like out-of-plane distances are recovered. Interestingly, the in-plane bond lengths within the bilayers show a stronger thickness-dependent change. The in-plane distortion in the center of the 5-bilayer structure is reduced compared to the bulk value. The step to the two and one bilayer models significantly reduces the distortion further and the structure transitions toward the more symmetric Cmcm structure. This behavior has been reported multiple times for SnSe[85,86] indicating that confinement effects can play a role in stabilizing a net of symmetric *p*–*p* orbital chains in the in-plane direction. This enables metavalently bonded chains in the bilayers along the p_x and p_y orbitals, while the out-of-plane bonding is still composed of covalent p_z bonds in the bilayer and van der Waals bonds in between. For the slabs of the initially rhombohedral materials, the situation is vastly different. Both SnTe and GeTe are stable in the polar orthorhombic phase in thin film slabs. For the surface bilayers, the strongest buckling can be seen, but instead of recovering the bulk-like out-of-plane distances for the inner layers, the structure gradually shifts to a cubic-like out-of-plane arrangement over the course of approximately five bilayers, so that both the buckling and the short/long interlayer distortion is suppressed in the center. This increase in symmetry in the center of the slabs is accompanied by lower buckling in the in-plane direction as well, leading to in-plane distortions above the bulk values. To study the origin of the equal bond distances at the slab center, the impact of depolarizing fields on the structure was tested. By replacing the surface Te atoms with 'pseudo' Te atoms with a fractional charge, the displacement field inside the slab was countered. As a result, the gaps between the bilayers and buckling within the layers are persistent even in the center of the relaxed structure.[84] It is remarkable, how gradual structural changes can be realized in the MVB compounds and that visible distortions persist up to 8–10 atomic layers away from the surfaces.

The changes in the atomic arrangement are also reflected in the bonding indicators (primarily the number of electrons shared) and intrinsic material properties, such as the dielectric

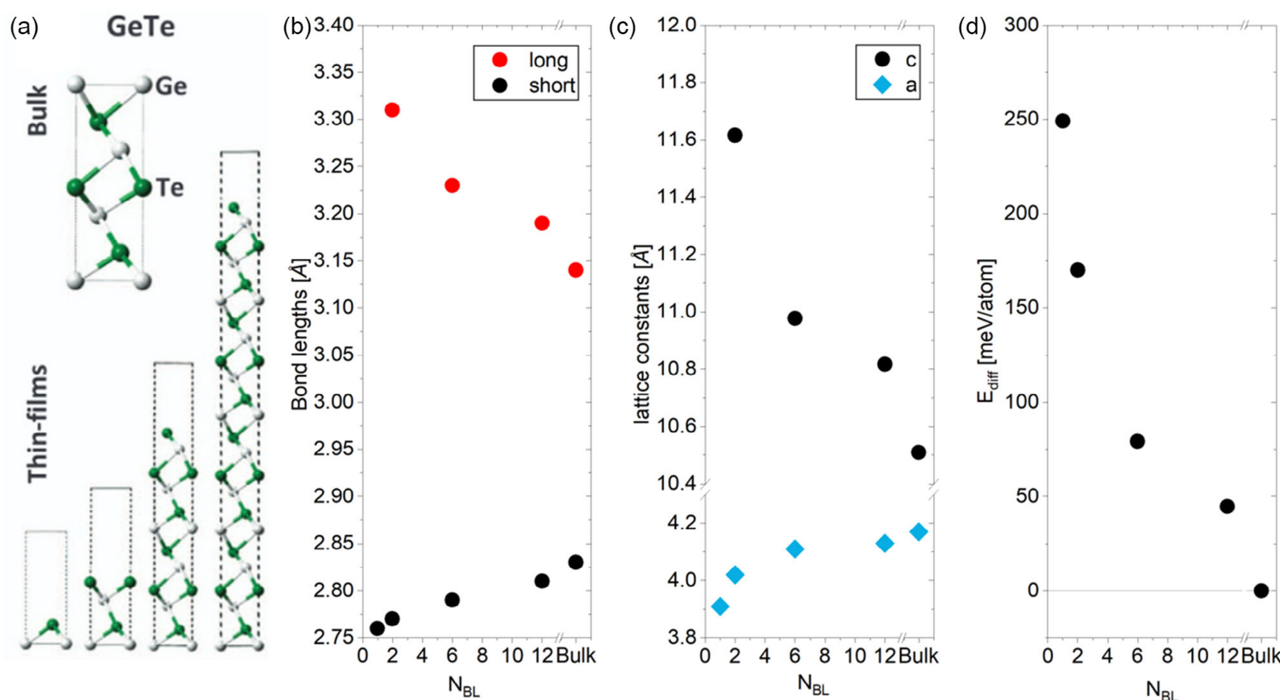

Figure 11. Structure of freestanding GeTe slabs in the (111) direction.[48] a) Side view of the unit cells of 1, 2, 6 and 12 bilayer films. b) Evaluation of the average bond lengths. The ultrathin films are more distorted, compared to the 12 BL and the bulk. c) Evaluation of in-plane and out-of-plane lattice parameter. The unit cell of the freestanding films of GeTe is compressed in-plane and elongated out-of-plane. d) Energy difference per atom for the different slabs. As the films get thicker, a less distorted state with more electron delocalization becomes energetically favorable; Reproduced with permission. (a) Reproduced under the terms of the CC BY 3.0 license.[48] Copyright 2017, The Authors. Published by Springer Nature. (b–d) drawn from tables in ref. [48].

© 2024 The Authors. physica status solidi (a) applications and materials science published by Wiley-VCH GmbH

18626319, 2024, 22, Downloaded from https://onlinelibrary.wiley.com/doi/10.1002/pssa.202300921 by Forschungszentrum Jülich GmbH Research Center, Wiley Online Library on [21/11/2024]. See the Terms and Conditions (https://onlinelibrary.wiley.com/terms-and-conditions) on Wiley Online Library for rules of use; OA articles are governed by the applicable Creative Commons License

18626319, 2024, 22, Downloaded from https://onlinelibrary.wiley.com/doi/10.1002/pssa.202300921 by Forschungszentrum Jülich GmbH Research Center, Wiley Online Library on [21/11/2024]. See the Terms and Conditions (https://onlinelibrary.wiley.com/terms-and-conditions) on Wiley Online Library for rules of use; OA articles are governed by the applicable Creative Commons License

function. This is shown in **Figure 10**. The gradual change from paired bilayers toward equidistant layers is visible also in the number of electrons shared (ES) within the bilayers. Going toward the center, this number decreases and approaches the cubic limit (lower horizontal line). On the surfaces of the film slab, on the contrary, the system is more distorted than bulk GeTe (higher horizontal line), in line with the increased ES value. Contrary to this, GeSe shows only the increased ES at the surface, and an otherwise flat value equal to the bulk value throughout the interior of the films. As the films become thinner, the ES values at the edges increase slowly for GeTe, but not for GeSe. The in-plane ES of GeTe settles above the bulk value for all besides the 1 bilayer film. For the GeSe films, the value is close to the bulk value, but the thinnest slabs show even values below the bulk value. These changes in bonding are closely related to changes in electron localization and properties with film thickness. The diagonal in-plane component of the static permittivity tensor is shown in Figure 10c. The increased in-plane localization leads to $\epsilon_{xx/yy}$ values below the bulk values, while the decreased localization in the less distorted GeSe films leads to an increase for the ultrathin slabs. It is striking that the lattice of [100] oriented GeTe and SnTe films is able to include such changes even for film thicknesses of 6 nm, i.e. 10 bilayers. This finding creates two new questions, which will be discussed in the following: Firstly, one can ponder if similar changes in the atomic arrangement and bonding also occur for other orientations of the films, such as the experimentally grown (111) direction and second, whether such changes will lead to measurable property changes.

In the (111) direction (hexagonal 0001), which is the growth direction observed for GeTe films on Si(111), the impact of the PD induced depolarization is even more pronounced, as the distortion direction is (anti-) parallel to the growth direction. The surface of such slabs can be studied if a cubic GeTe stack with the same termination on both surfaces is considered in the calculations, in which the center atoms are fixed and the outer layers are relaxed.[87] This creates a structure with an increased rhombohedral distortion and shift of Ge atoms toward the surface Te atoms. The frozen center serves as the infliction point of the distortion/domain boundary. Other surfaces than a pristine 1×1 Te termination yield a larger surface energy and are thus less favorable. Similar to the slabs of the (100) GeTe, the distortion at the surface is larger than in bulk GeTe. Layer thickness-dependent results up to 12 bilayers, albeit only from single domain slabs[48] are shown in **Figure 11**. With increased

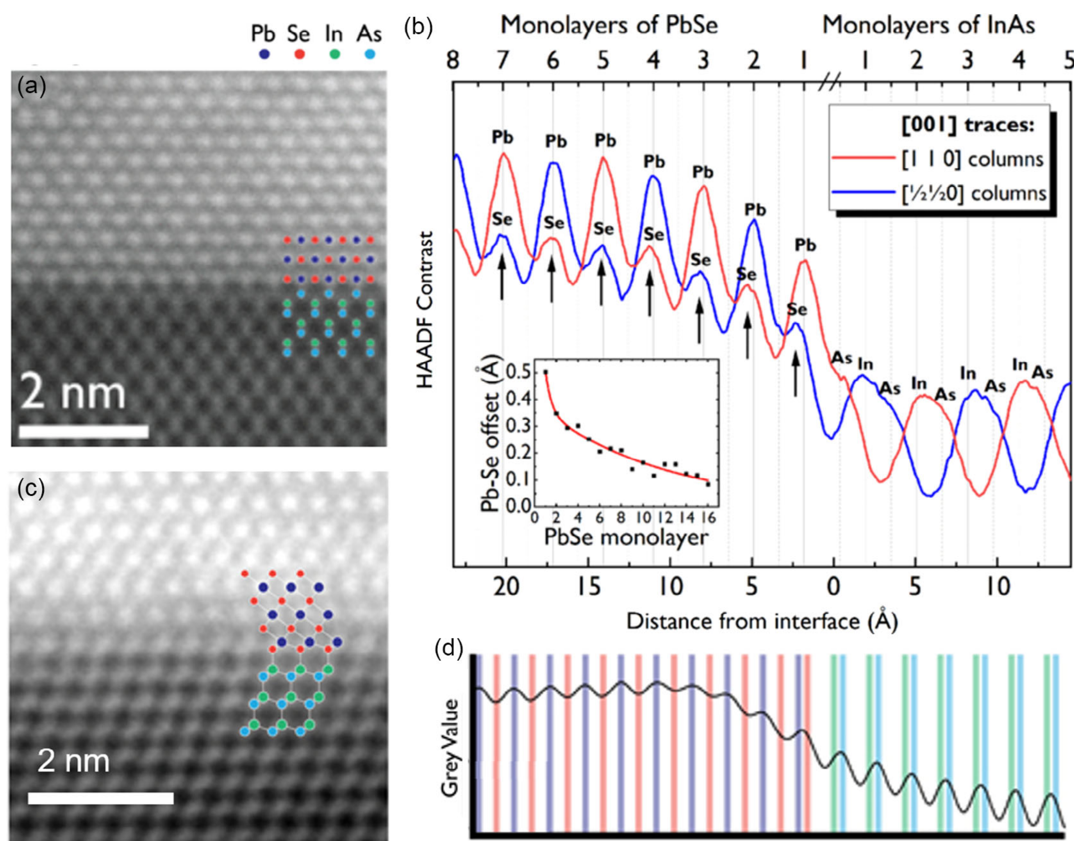

Figure 12. Interfaces of PbSe on InAs (100) (top) and InAs(111) (bottom). a) HAADF-TEM image of the interface on InAs (100). The PbSe adapts the growth direction of InAs. b) evaluation of the HAADF contrast on traces normal to the interface. For (100) growth of PbSe, the layers near the interface show a buckling with a measurable offset up to 0.5 Å, which gradually relaxes but is still visible 16 monolayers inside. c) HAADF-TEM image of the interface on InAs(111). The PbSe adapts the growth direction of InAs. For the (111) direction, especially the first bilayer is distorted. d) line plot of a wide integrated line trace normal to the interface, more clearly showing the distortion at the interface. (a,b) Reproduced with permission.[89] Copyright 2020, American Physical Society. (c,d) Reproduced with permission.[88] Copyright 2021, American Vacuum Society.

© 2024 The Authors. physica status solidi (a) applications and materials science published by Wiley-VCH GmbH

physica status solidi a
www.pss-a.com

confinement, the out-of-plane lattice constant increases, while the in-plane lattice constant decreases. Regarding the atomic positions within the unit cell, the PD increases, as the short bonds decrease, while the long bonds increase. Looking at the energy difference per atom in the different slab models (**Figure 12**d), the thinnest films show an increased energy by 250 meV $atom^{-1}$. As lowering the energy per atom through electron delocalization along the orbital chains is no longer feasible for the thin films with a finite chain length (i.e., only 4*p* orbitals overlap in the 2 Bilayer (BL) slab). Instead,the relaxed structures have a higher degree of PD and thus more localization between adjacent atoms.

Experimentally, freestanding slabs of such small thicknesses are prone to oxidation and difficult to measure. However, the effect of the depolarizing fields should also be visible for interfaces of such chalcogenides with insulators/dielectrics and/or surfaces. In PbSe films grown lattice-matched on III–V surfaces a distortion gradient can be seen for films both with (111) and (100) direction parallel to the substrate surface.[88,89] Like SnTe, PbSe still has a cubic stable phase at room temperature,[90] but due to the larger differences in atomic masses and radii, separation of the atomic species in TEM images is easier to achieve. In Figure 12, the interfaces of PbSe grown on InAs(100) and (111) surfaces are shown. From the intensity traces along the different atomic columns (seen on the right side of the images), it becomes apparent that PbSe indeed shows a polarizing distortion (shift of the sublattices) that is largest at the interface and gradually disappears further inside the film. A slight offset can still be seen even 16 monolayers inside for the (100) structure. On the (111) surfaces, one heavily shifted interface bilayer layer can be seen, after which the cubic structure is obtained.

These findings immediately raise the question, which atomic arrangement and properties are obtained for rhombohedral GeTe? From the perspective of suitable Si substrate terminations, i.e. 7×7, H and $\sqrt{3} \times \sqrt{3}$ Sb, the last seems to be the best choice, at first glance. GeTe on 7×7 or H termination grows amorphous in the first layers and spontaneously crystallizes after a certain thickness of about 3 nm has been reached,[48] whereas a crystalline film directly forms on top of the $\sqrt{3} \times \sqrt{3}$ Sb termination. Despite being crystalline from the start, Raman active modes appear only at and above 4 bilayers.[91] This could be explained either by a phase transition from a cubic phase toward the rhombohedral phase, or intermixing of the Sb into the GeTe. As TEM images of the interface show a bright passivation layer (cf Figure 3), the first hypothesis seems more likely. However, a new study combining STM and angle-dependent X-ray photoelectron spectroscopy (XPS) suggests that the Sb from the termination acts as a surfactant and is still present at the surface of GeTe up to 5 nm thick films.[34] The Raman modes of disordered rock salt GeSbTe are forbidden,[92] therefore Raman modes would only appear after GeTe bilayers are formed.

On the 1×1 Si or 7×7 reconstructed Si (111) surfaces, GeTe films initially grow amorphous. This phenomenon has been denoted as a "blackout" due to the loss of the intensity of the RHEED reflexes at the early stages of growth, as shown in **Figure 13**. Only after a critical thickness, crystallization occurs and an epitaxial film is recovered, resulting in clearly discernible RHEED reflexes.[25,48,93] The temperature dependency of this blackout was studied for SnTe growth at different substrate temperatures. As the crystallization temperature of bulk SnTe is lower than for GeTe, a temperature regime is accessible for SnTe which is far away from the desorption temperature

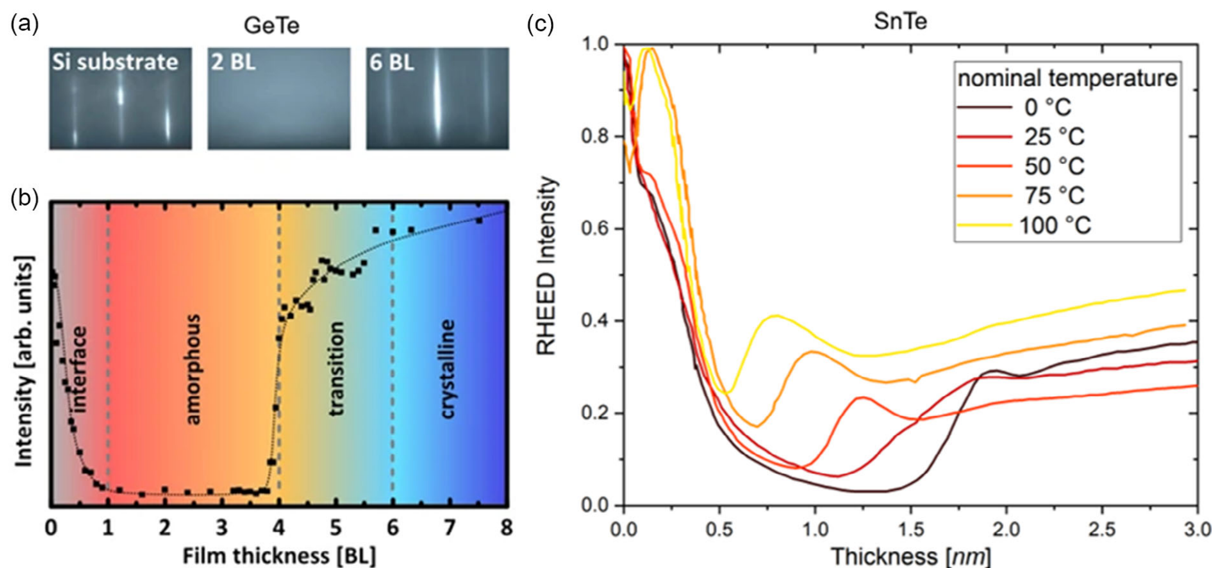

Figure 13. Blackout phenomena in GeTe and SnTe. a) RHEED images at different stages of GeTe growth. The crystalline reflexes and the specular spot disappear for the amorphous region, causing a "blackout" of the RHEED image. b) Integrated RHEED intensity during growth around the GeTe(111)–(1×1) reconstruction streaks as function of thickness. A critical thickness can be defined, at which the film crystallizes. c) integrated Intensity of the specular spot during SnTe growth as function of thickness. The loss of the RHEED intensity during the initial amorphous film growth and subsequent spontaneous crystallization is visible for both compounds. At higher temperatures, the critical thickness for crystallization is lower. (a,b) Reproduced under the terms of the CC BY 3.0 license.[48] Copyright 2017, The Authors. Published by Springer Nature. (c) redrawn from ref. [93].

© 2024 The Authors. physica status solidi (a) applications and materials science published by Wiley-VCH GmbH

18626319, 2024, 22, Downloaded from https://onlinelibrary.wiley.com/doi/10.1002/pssa.202300921 by Forschungszentrum Jülich GmbH Research Center, Wiley Online Library on [21/11/2024]. See the Terms and Conditions (https://onlinelibrary.wiley.com/terms-and-conditions) on Wiley Online Library for rules of use; OA articles are governed by the applicable Creative Commons License

18626319, 2024, 22, Downloaded from https://onlinelibrary.wiley.com/doi/10.1002/pssa.202300921 by Forschungszentrum Jülich GmbH Research Center, Wiley Online Library on [21/11/2024]. See the Terms and Conditions (https://onlinelibrary.wiley.com/terms-and-conditions) on Wiley Online Library for rules of use; OA articles are governed by the applicable Creative Commons License

of Te. It was shown that the critical thickness for crystallization is decreasing as the growth temperature increases. Furthermore, a sample where growth stopped in the blackout region (0.9 nm for 0 °C substrate temperature) could be crystallized after heating to 50 °C (at which the critical thickness is ≈0.9 nm). This implies that the blackout effect is a manifestation and viable probe of the increased crystallization temperature for ultrathin films[58] as discussed previously.[7]

The evolution of the structure of GeTe films above the critical thickness was probed by X-ray diffraction[51] and is summarized in **Figure 14**. In addition to the Θ–2Θ measurements presented already in Figure 2, rocking curves and reciprocal space maps of the 000 L peaks were measured to obtain the total scattering intensities of the GeTe bilayers. The experimental intensity ratios were compared to calculated intensities based on structure factor calculations of a distorted rock salt phase, adjusted by a geometrical prefactor to include the angle dependent change in illuminated crystal volume. The modelled structure fits well to the simulation results for the free standing GeTe slabs shown in Figure 12. An increase in out-of-plane lattice constant, a decrease of the in-plane lattice constant and an increase in PD is visible for ultrathin films. The increase in the PD with decreasing film thickness is closely related to an increase in the number of the electrons shared in the short Ge-Te bonds. This change in chemical bonding can be interpreted as an increase in the covalency of the metavalent bonds.

For sesqui-chalcogenides like Sb_2Te_3, the structure is more complex due to the formation of quintuples instead of bilayers.

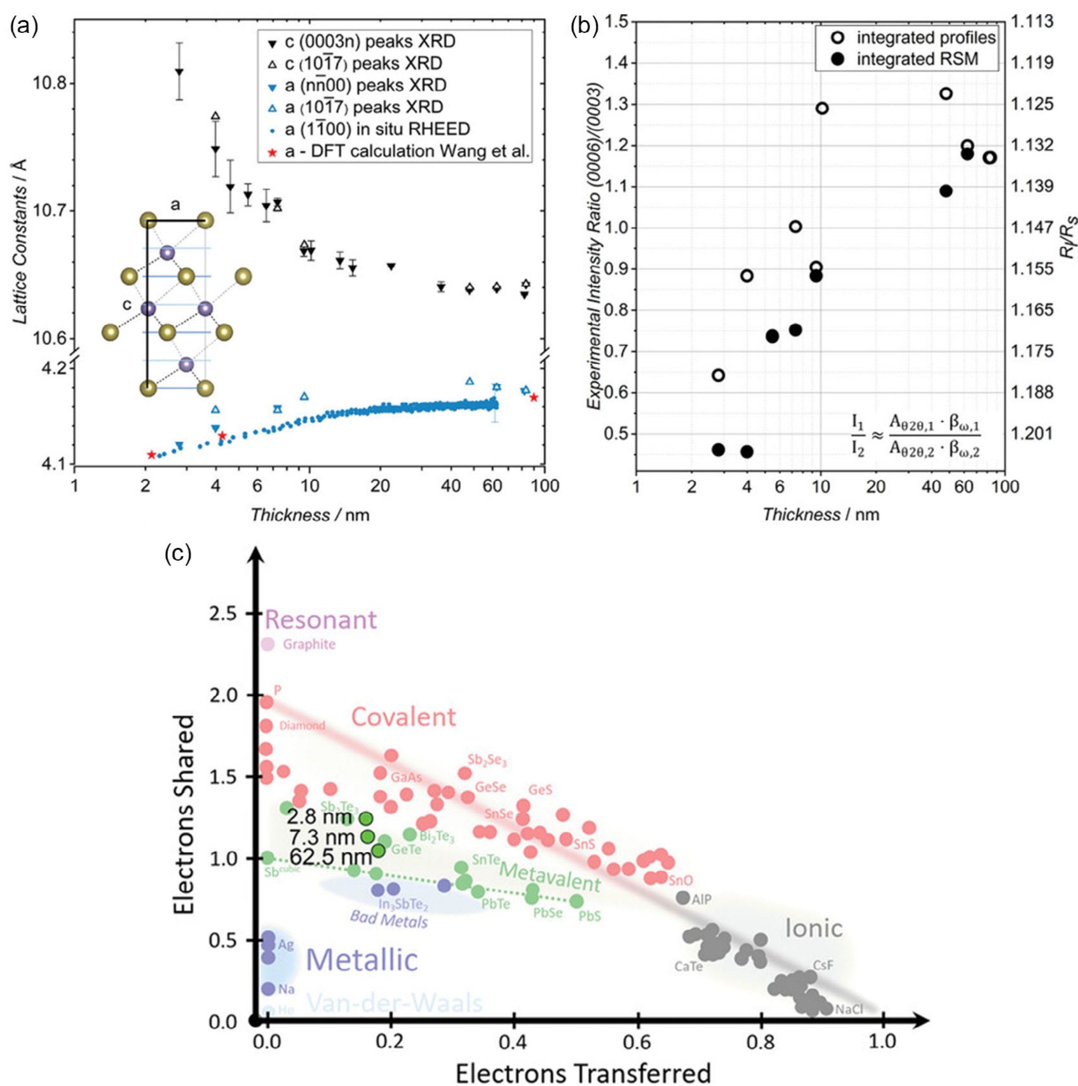

Figure 14. Confinement effect on structure and bonding in (0001) oriented GeTe films. a) Shift of the out-of-plane and in-plane lattice constant. Just as in the freestanding slab calculation, the unit cell is compressed in-plane and expanded in out-of-plane direction b) Experimentally determined intensity ratios dependent on the film thickness. For thinner films, the intensity ratio is decreased and the average distortion is increased. c) Location of 3 films of different thickness in the ES/ET Map. The thinner and more distorted films have a larger degree of electron sharing. Reproduced with permission.[51] Copyright 2022, Wiley-VCH GmbH.

© 2024 The Authors. physica status solidi (a) applications and materials science published by Wiley-VCH GmbH

18626319, 2024, 22, Downloaded from https://onlinelibrary.wiley.com/doi/10.1002/pssa.202300921 by Forschungszentrum Jülich GmbH Research Center, Wiley Online Library on [21/11/2024]. See the Terms and Conditions (https://onlinelibrary.wiley.com/terms-and-conditions) on Wiley Online Library for rules of use; OA articles are governed by the applicable Creative Commons License

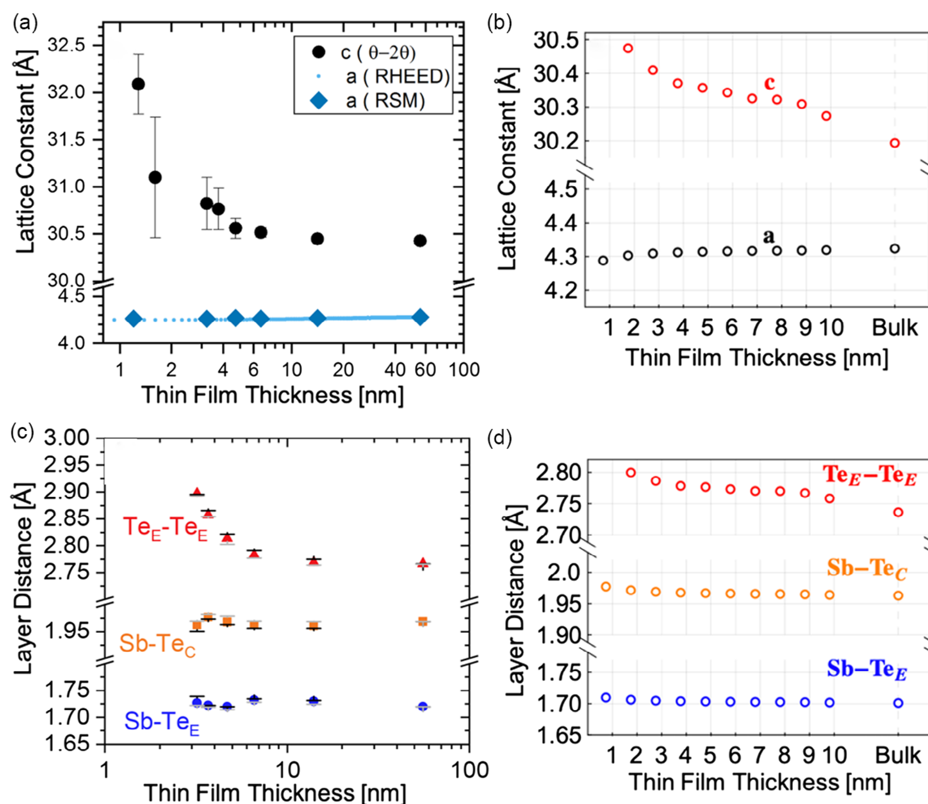

Figure 15. Structural changes in Sb_2Te_3 with thickness. a,b) lattice constants from DFT calculations and MBE grown films, respectively. For both, the in-plane lattice constant stays the same, while the out-of-plane lattice constant is increased for ultrathin films. c,d) Layer distances obtained from DFT calculation and simulation of the XRD patterns. The increase in the out-of-plane lattice constant stems from an increase in the pseudo van der Waals gap between the quintuples. Reproduced with permission.[63] Copyright 2023, Wiley-VCH GmbH.

Again, a high symmetry reference structure can be defined as a perfect octahedral arrangement with a Sb–Te–Sb–Te–Te–Sb stacking sequence, shown in **Figure 15**a The quintuple structure can be recovered by shifts of atomic planes if two parameters are used, coined Decoupling (as it splits the quintuple layers) and Peierls (as it is responsible for the bond length ratio within the Quintuples)[63]

With a similar method as for GeTe,[51] the two parameters were extracted from a combination of diffraction simulations and reciprocal space maps of the 000 L peaks. The resulting lattice parameters and layer distances are shown in Figure 15b,d. They fit quite well to the average values from an accompanying DFT calculation shown in Figure 15c,d. In both cases, the gap between the quintuples increases compared to the bulk, while the bonds inside the quintuples only show minor changes.

The chemical bonding analysis in **Figure 16** shows that the short Sb–Te bonds become stronger (and shorter) at the surface, while they approach their bulk value inside the film.[63] The increase in the gaps and resulting diminishing of ES through the gap is independent whether it is at the surface or the center of the slab. For layer slabs that are thin enough, the bonding contributions between the quintuples are sufficient to couple the top and bottom surface states of these materials, thereby losing the topological protection. This effect, also called quantum interference has been shown through angle resolved photoelectron spectroscopy (ARPES) measurements in Bi_2Se_3 and Sb_2Te_3 in films below five quintuples.[31–33] Along with the changes in structure and bonding of the ultrathin chalcogenides, a number of material properties are changing as well, which are quite relevant for the application of these films. These properties will be briefly presented and discussed next.

3.2. Dependence of Optical Properties on Film Thickness

The intrinsic optical properties of materials, such as the band gap E_{gap} and the shape of the dielectric function are closely linked to the electronic band structure, and therefore also the bonding of the films. Because these properties are measurable with non-destructive methods and no further sample processing is needed to obtain optical data, studying the interaction of light with ultrathin films is a promising method to study confinement effects, even though the interacting material volume becomes limited upon confinement.

The effect of confinement on the band gap of chalcogenide films is studied theoretically on freestanding thin film slabs and shown in **Figure 17**a,c. For conventional semiconductors such as GeSe or SnSe, a $1/d^2$ proportionality is expected and found due to quantum confinement. This thickness dependence can be explained due to the parabolic bands used in the effective

© 2024 The Authors. physica status solidi (a) applications and materials science published by Wiley-VCH GmbH

18626319, 2024, 22, Downloaded from https://onlinelibrary.wiley.com/doi/10.1002/pssa.202300921 by Forschungszentrum Jülich GmbH Research Center, Wiley Online Library on [21/11/2024]. See the Terms and Conditions (https://onlinelibrary.wiley.com/terms-and-conditions) on Wiley Online Library for rules of use; OA articles are governed by the applicable Creative Commons License

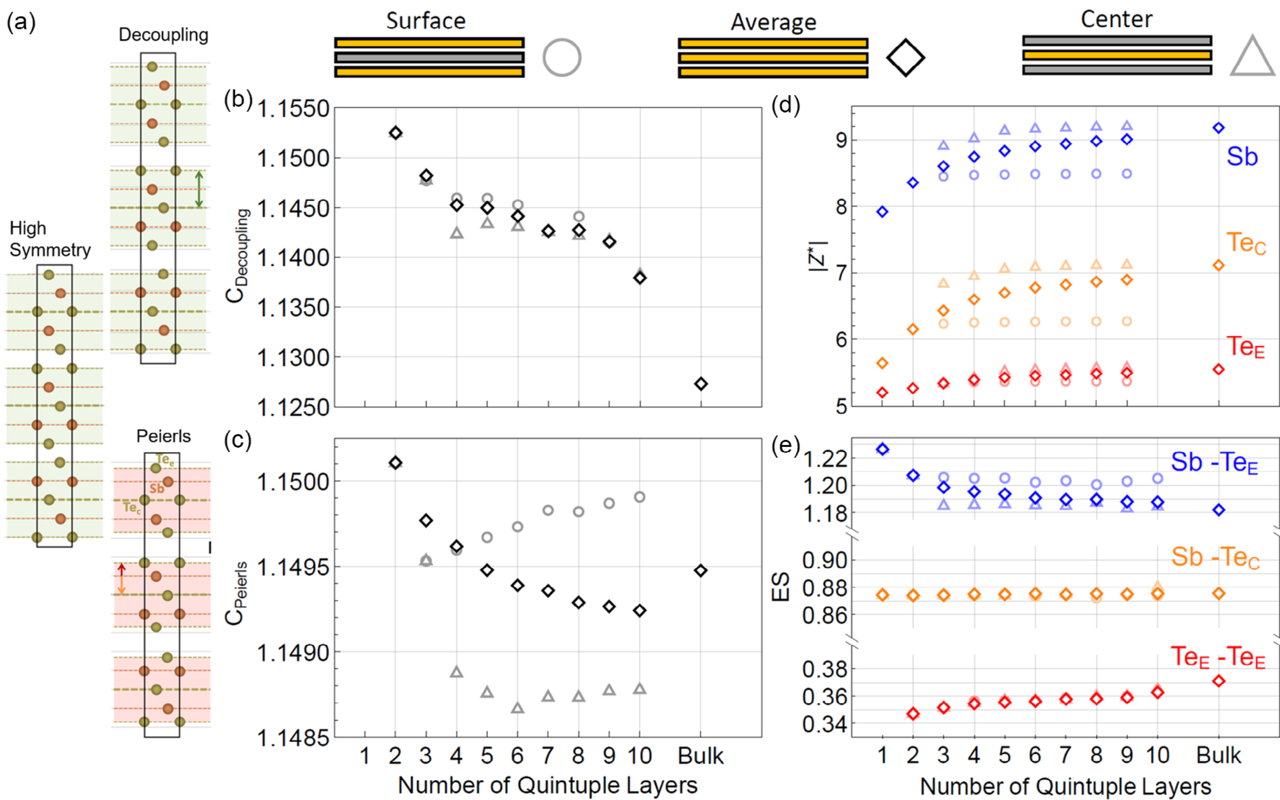

Figure 16. Change of bond indicators and properties in Sb_2Te_3. a) Sketch of the distortion patterns from a virtual high symmetry state. Two distortion motifs are required to obtain the Sb_2Te_3 quintuple structure. b,c) magnitude of the two distortion parameters needed to describe the Sb_2Te_3 structure. While the coefficient linked to decoupling of the quintuples is equally increased at the surface and the center for thinner films, the coefficient linked to distortions in the quintuple shows subtle differences between the surface and the central quintuple. On average, both increase. d) The Born effective charge Z* for the different atomic sites inside Sb_2Te_3. The value at the center is always larger than the value at the surface, but decreases below 5 quintuples. e) Electrons shared value for the different bonds within the Sb_2Te_3 film. ES between Sb and the central Te atom is constant for all thicknesses and all positions within the slabs. For the bond of Sb toward the Te edge atoms, the surface quintuple is more localized than the central one, as seen from the corresponding ES value. On average, ES increases for the thinnest films. The ES between the quintuples is decreasing for thinner films, independent on the position in the slab. Reproduced with permission.[63] Copyright 2023, Wiley-VCH GmbH.

masses theory.[94] By employing tight binding calculations to explore the electronic structure of PbSe quantum wells, instead, a 1/d proportionality has been found.[95] This was attributed to the mainly linear dispersion of the bands obtained for the *p–p* orbital chains. Such a thickness dependence is a consequence of an unusual form of quantum confinement directly related to the bonding in the material. This 1/d dependence is the reason for an extension of visible quantum confinement effects into larger thickness ranges and the higher magnitude of the change of the energy gap. The same bonding pattern, i.e., a chain of half-filled *p*-orbitals is also at work in mono chalcogenides like GeTe and SnTe. Concerning the freestanding monochalcogenide slabs discussed earlier,[84] it can be seen that both GeTe and SnTe show changes in the E_{gap} which extend to thicker films and show a large overall change. A kink in the slope of the GeTe and SnTe slabs can be seen at 6 BL and is explained by a change from an indirect band gap below 6 to a direct band gap at 6 BL and above. Fits of a 1/d behavior in the direct band gap region and a $1/d^2$ behavior in the indirect bandgap region can describe the data well. As only the direct band gap results from transitions along the *p–p* orbital chains, the indirect band gap shows the usual $1/d^2$ proportionality. Similar findings have also been reported for sesqui-chalcogenides such as Bi_2Se_3.[30,31] Both the bulk band gap and the gap opening for the surface states, as quantum interference starts to affect the topological protection, follow the same slope and can be fitted well with the 1/d behavior. For conventional semiconductors like GeSe and SnSe instead, the expected $1/d^2$ behavior fits the entire thickness range. As shown in Figure 17b,d, the peak of the optical transition of, for example, GeTe[51] and Bi_2Se_3[31] shifts with 1/d behavior as well. However, the shifts in the optical transitions are more pronounced. This implies that an additional effect is superimposed, which will be discussed in the following:

A prominent feature in the dielectric function of the metavalent chalcogenides (**Figure 18**) is the strong peak in the imaginary part of the dielectric function in the visible range. This peak arises from interband transitions, which are known to be strong in these compounds due to their large joint density of states (jDOS) and *p*-orbital overlap.[96] It has been shown that increased electron localization in thick films leads to a reduction

© 2024 The Authors. physica status solidi (a) applications and materials science published by Wiley-VCH GmbH

18626319, 2024, 22, Downloaded from https://onlinelibrary.wiley.com/doi/10.1002/pssa.202300921 by Forschungszentrum Jülich GmbH Research Center, Wiley Online Library on [21/11/2024]. See the Terms and Conditions (https://onlinelibrary.wiley.com/terms-and-conditions) on Wiley Online Library for rules of use; OA articles are governed by the applicable Creative Commons License

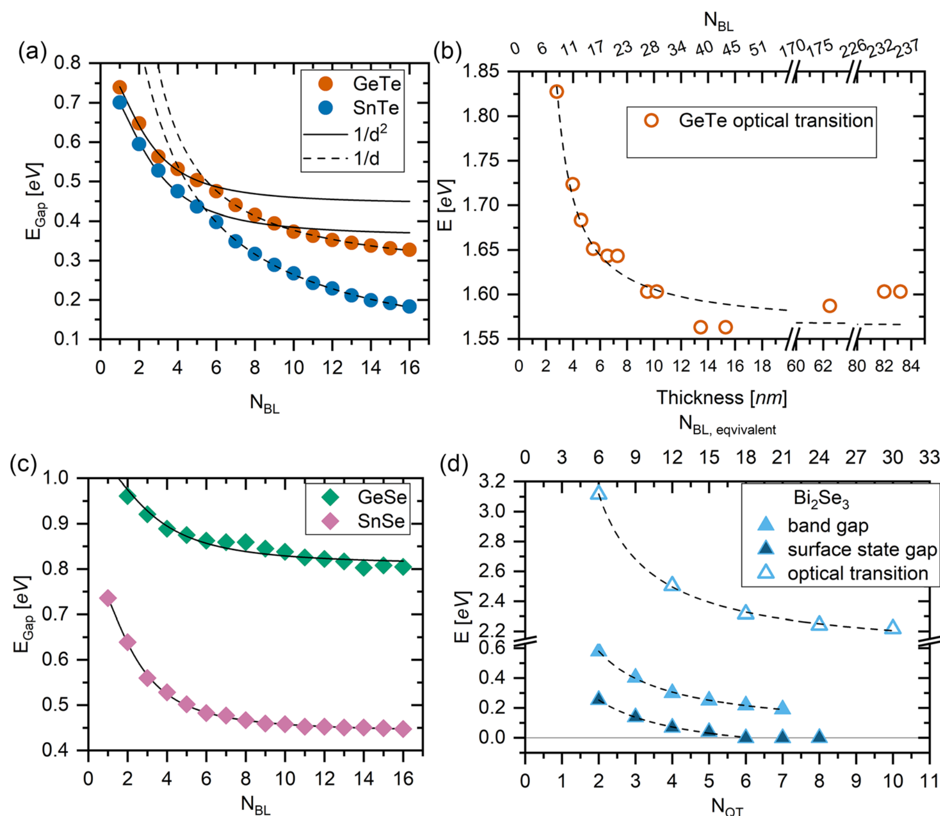

Figure 17. Dependence of optical properties on film thickness for several different chalcogenides. a) Calculations for the two metavalent materials GeTe and SnTe show a 1/d proportionality for thicker samples and a $1/d^2$ proportionality of the band gap for thinner films. b) the 1/d proportionality fits to experimental data of the maximum of the optical transition in GeTe. c) for GeSeand SnSe a $1/d^2$ proportionality fits the entire thickness range of the slab. d) For metavalent sesqui-chalcogenides such as Bi_2Se_3, a 1/d proportionality can be fitted to experimental data of the band gap, surface state gap and optical transition. (a,c) redrawn from ref. [84], (b) from ref. [51], and (d) from refs. [30,31].

of the peak height.[96] Since the integral of the dielectric function has to be conserved (sum rule for optical transitions) as long as the number of electrons per unit cell involved in the optical transitions is fixed, a concomitant blueshift of the peak will occur.

With decreasing film thickness, the electron localization inside the films increases, as seen from the increasing ES value. In turn, the maximum of the dielectric function should decrease. This behavior is seen experimentally for Sb,[97,98] GeTe,[51] and Bi_2Se_3.[31] An optical anisotropy is predicted in (100) oriented MVB monochalcogenides, as only one chain is affected by the transition, leading to a decoupling of the optical response for *p*- and *s*-polarized waves.[95] The corresponding shift (and reduction in intensity) of the optical response due to the reduction of film thickness can also be taken as a rough benchmark for the impact of pure confinement (without distortion). After 10 bilayers or 3 nm of PbSe, the bulk dielectric function is recovered if no distortion is considered. In the experimentally determined dielectric functions, the bulk dielectric function is recovered only after roughly 10 nm. Therefore, the thickness-induced distortions and bonding changes will affect the properties of the material in addition to normal quantum confinement.

3.3. Dependence of Vibrational Properties on Film Thickness

The structural distortion in thin films and the change of the bond strengths affect the phonon modes as well. From the results presented in **Figure 19**, two trends can be seen. First, the crystals which form a bilayer structure in (0001) direction (i.e., GeTe[48,51,91,99] and Sb,[98] Figure 19a,b) show a phonon hardening of both E_g and A_{1g} modes. This can be explained by an increased bond strength of the short bonds inside the bilayers, as the thinner films are more heavily distorted. For the layered chalcogenides with n-tuple stacking along the (0001) direction (Sb_2Te_3[63] and Bi_2Se_3,[100,101] Figure 19c–e) instead a phonon softening can be observed for the A_{1g} mode. In this mode, the outer V–VI layers of the tuples are oscillating in sync away from the central VI atom and toward the next tuple. The softening at low thicknesses is attributed to the decreased restoring force at the gap for low thicknesses.[63] For Sb_2Te_3 also a phonon hardening of the A1g2 mode can be seen. This vibration probes the bond strengths of the Sb-Te_{edge} bond as well, which is mainly affected by increased distortions within the quintuple. For Bi_2Se_3, the A1g2 mode remains constant, which implies only a decoupling of the quintuples without further intra quintuple

© 2024 The Authors. physica status solidi (a) applications and materials science published by Wiley-VCH GmbH

18626319, 2024, 22, Downloaded from https://onlinelibrary.wiley.com/doi/10.1002/pssa.202300921 by Forschungszentrum Jülich GmbH Research Center, Wiley Online Library on [21/11/2024]. See the Terms and Conditions (https://onlinelibrary.wiley.com/terms-and-conditions) on Wiley Online Library for rules of use; OA articles are governed by the applicable Creative Commons License

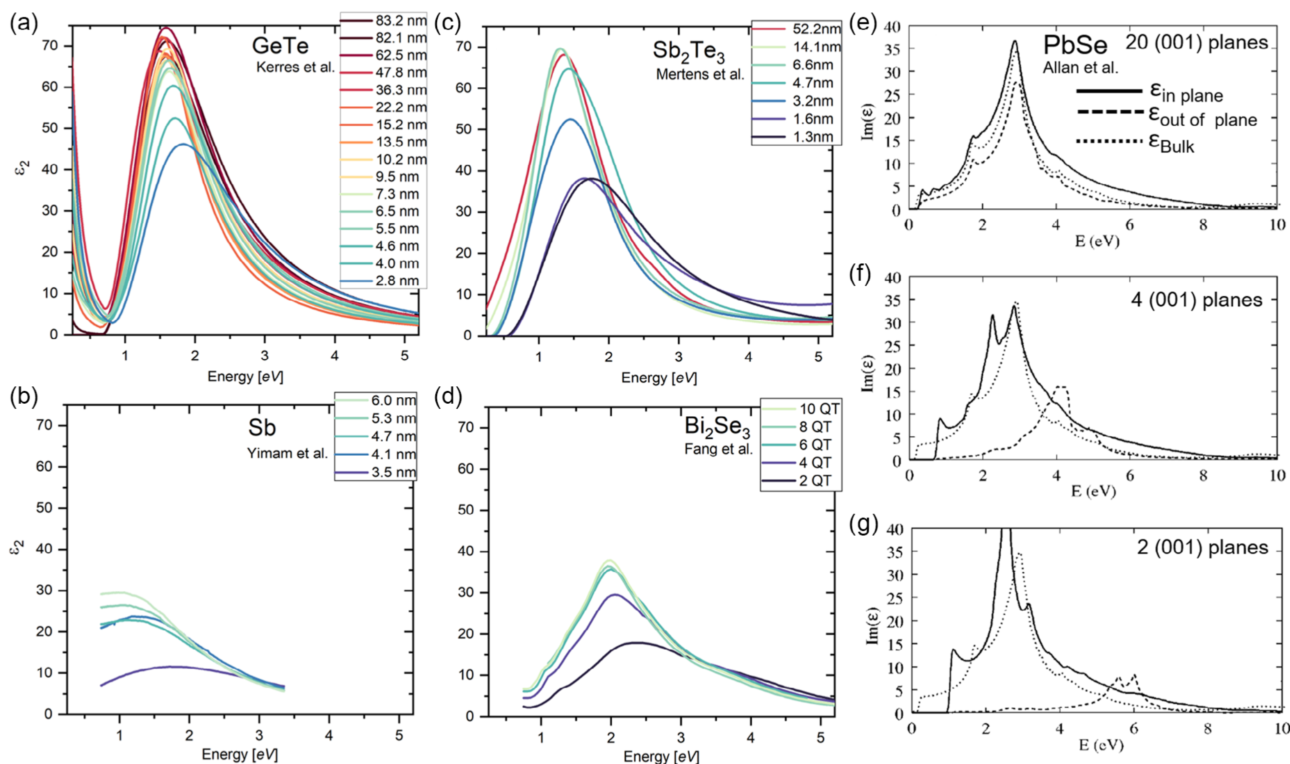

Figure 18. Imaginary part of the dielectric functions of different chalcogenides as a function of film thickness. a) GeTe, redrawn from ref. [51]. b) Sb, redrawn from ref. [97]. c) Sb_2Te_3, redrawn from ref. [63]. d) Bi_2Se_3, redrawn from ref. [31]. e–g) tight binding calculation of the dielectric function of PbSe slabs with 20, 4 and 2 (001) planes, respectively. Reproduced from permission.[95] Copyright 2004, American Physical Society. All these materials are governed by a large peak of the imaginary part of the dielectric function at around 2 eV. For increased confinement/ultrathin films the peak decreases in intensity and shifts to higher energies. The calculated dielectric function of PbSe resolves the in-plane and out-of-plane part of the dielectric tensor and shows that primarily the out-of-plane part decreases and blueshifts for PbSe in (001) orientation.

distortions. Similar experiments on GST[102] show that the behavior is persistent for ternary layered materials as well.

3.4. Devices Based on Ultrathin Films

In the last part of the review, recent advances in the use of ultrathin PCM layers for device application are covered. Besides the proposed use of confined Sb films as electrical switches in 2018,[103] electrically switched devices based on ultrathin Sb_2Te_3 (4 nm)[104] and GeTe (10 nm)[105] have been published recently. Their performance is depicted in **Figure 20**. Both materials have a lower performance in thicker devices as compared to GST225 devices. Bulk Sb_2Te_3 has a crystallization temperature around room temperature, leading to low retention, while GeTe shows a slow, growth dominated crystallization with high crystallization and high melting temperatures. Still, their confined counterparts both perform better than reference GST cells in terms of set speed and reset power consumption. The reason for this behavior can be found in the confinement itself, but also in the interplay with the surrounding interfaces. This interaction can affect the crystallization temperature T_c of the phase change materials upon confinement to ultrathin films differently.[106] From the increased potential energies of the freestanding ultrathin models (cf. Figure 11d), an increase in T_c is expected. For TiN electrodes, this increase in T_c is also visible in devices. The Sb_2Te_3 bridge cell was sandwiched between TiN layers, which shifts the low T_c of Sb_2Te_3 toward feasible values.[104] At the same time, the bridge structure allows for confinement to ultrathin layers without risking leakage currents. The 10 nm GeTe device was instead fabricated like a T-shaped device with a W electrode. Contrary to TiN, W leads to a reduction of the crystallization temperature for ultrathin films,[106] which makes a SET operation possible below 3 V at a pulse length of 6 ns. The RESET operation can be performed below 4 V with a pulse length of 50 ns. This speeds up the process and reduces the power consumption of the RESET by an order of magnitude.[105] With this device, a lower value for the reset current density than the recently published superlattice structures with minimal supercell thicknesses[107] has been reported. Yet, the device still possesses an unfavorable large drift coefficient. As one reason for the decreased power consumption, an increased heat confinement inside the GeTe film[105] has been suggested. The idea of an improved heat confinement to engineer better results is a general trend in current research. If ultrathin GST is spaced between W

© 2024 The Authors. physica status solidi (a) applications and materials science published by Wiley-VCH GmbH

18626319, 2024, 22, Downloaded from https://onlinelibrary.wiley.com/doi/10.1002/pssa.202300921 by Forschungszentrum Jülich GmbH Research Center, Wiley Online Library on [21/11/2024]. See the Terms and Conditions (https://onlinelibrary.wiley.com/terms-and-conditions) on Wiley Online Library for rules of use; OA articles are governed by the applicable Creative Commons License

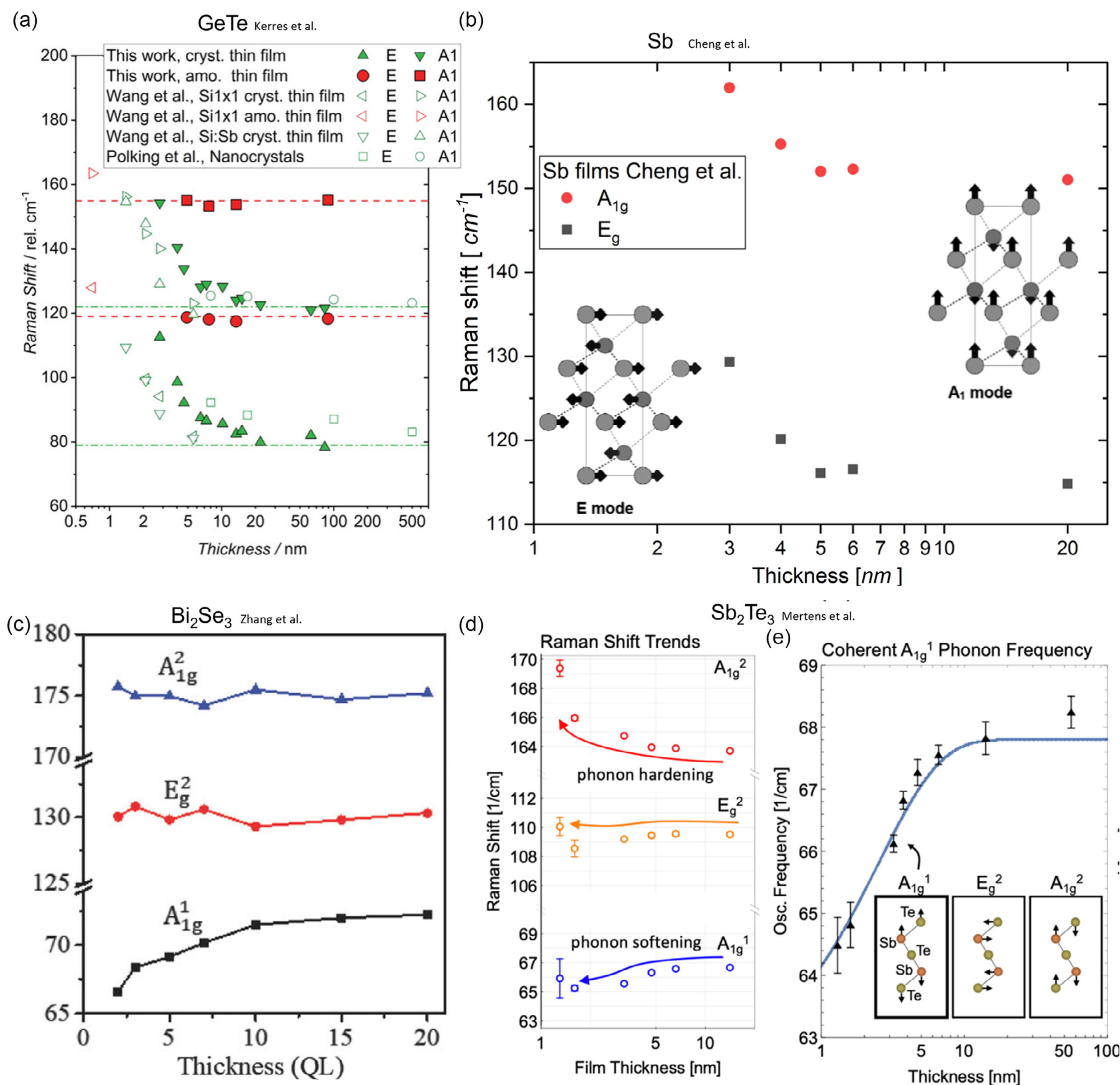

Figure 19. Phonon frequencies of different chalcogenides as a function of film thickness. a) Phonon frequency of A_{1g} and E_g mode of crystalline and amorphous GeTe films as a function of thickness. For crystalline GeTe, both A_{1g} and E_g mode frequencies increase for ultrathin films below 10 nm, while no shift is visible in amorphous GeTe films. The strongest increase is visible below 5 nm film thickness. b) crystalline Sb. A mode strenghtening is observed below 5 nm in Sb as well. c) crystalline Bi_2Se_3. The A1g1 mode frequencies decrease for films below 10 nm, while the other modes stay constant. c,d) Raman and coherent phonon spectroscopy of Sb_2Te_3. The A1g1 mode frequency decreases for thinner films. In contrast to Bi_2Se_3, the A1g2 mode increases for thinner films. (a) Reproduced with permission.[51] Copyright 2022, Wiley-VCH GmbH (b) redrawn from ref. [98]. (c) Reproduced with permission.[100] Copyright 2011, American Chemical Society. d,e) Reproduced with permission.[63] Copyright 2023, Wiley-VCH GmbH.

layers, the thermal boundary conductance is reduced, which in turn reduces the RESET current of the devices by 50%.[108] The increase in the PD in very thin films of chalcogenides will also affect the property portfolio of the film. For the ultrathin Sb_2Te_3 devices, a reduced resistivity ratio between the amorphous and the crystalline phase has been reported.[22,24,37,49] As the Joule heating generated by the (RE)SET currents is proportional to the film's resistance, the doubled resistance in the SET state will also create twice as much heat at the same current. If such devices can also demonstrate a high cyclability, they present a promising avenue to implement ultrathin films in memory applications.

© 2024 The Authors. physica status solidi (a) applications and materials science published by Wiley-VCH GmbH

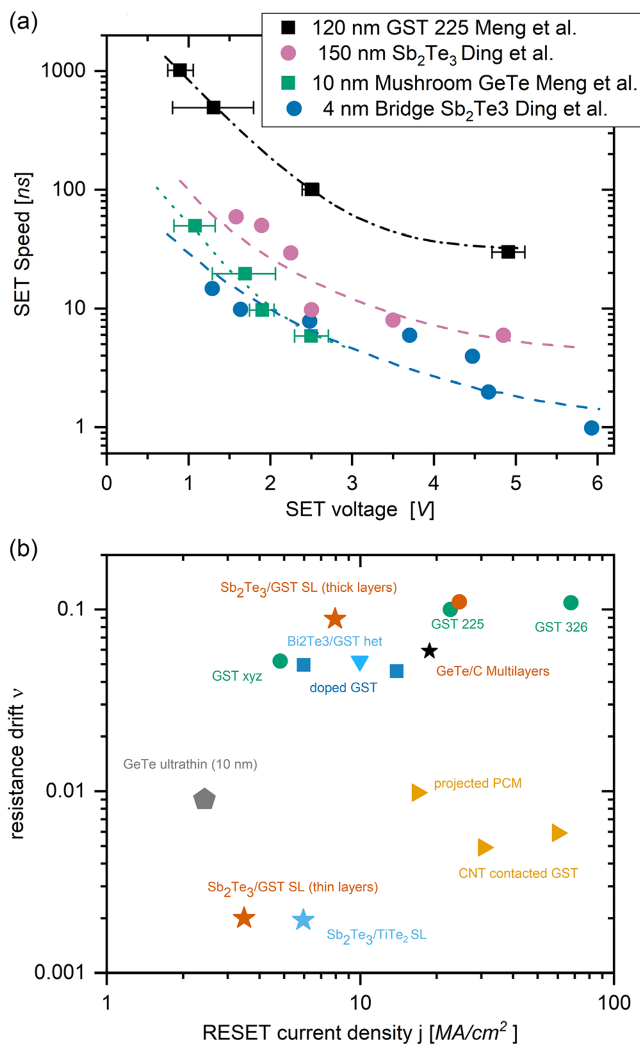

Figure 20. a) Set speed and set voltage for ultrathin GeTe and Sb_2Te_3 devices compared to thick reference devices. Redrawn from refs. [104,105]. b) location of the ultrathin GeTe devices in the resistance drift vs. RESET current density plot. Redrawn from refs. [107,114–123].

4. Conclusion & Outlook

The present review compares and summarizes recent findings and developments regarding the growth of textured chalcogenide films in general, and the confinement to ultrathin films in particular. In the first part, the growth of chalcogenides on different surface terminations of Si(111) is discussed. In addition to the reported epitaxial growths of GeTe and Sb_2Te_3 on 1×1, 7×7, and $\sqrt{3} \times \sqrt{3}$ Sb:Si, growth on Te interfaces is promoted, both for epitaxial and fiber-textured growth on amorphous Si or SiOx.[40] This, in combination with other two-step growth methods, such as Sb_2Te_3[57] or Antimonene[67] seeds, overcomes the substrate limitations regarding highly textured films and serves as a good entry for the use of textured films in devices. It has been shown that recrystallization in GeSbTe films from a highly textured interface is able to provide fast crystal growth and recovers the original orientation of the grain, improving on the reproducibility due to the lack of random grain boundaries.[14] While the general growth direction of the crystal is recovered, the degree of atomic ordering is lowered compared to the crystalline matrix, either by an increased amount of antisite defects or a lower degree of vacancy ordering in the recrystallized films.[39] Yet, these are general effects that can happen in each phase transition. It is likely, that the lower volume of amorphized spots in electrically switched devices compared to the laser irradiation experiment shown here, mitigates these effects as well.

Regarding the confinement of ultrathin films, the peculiar characteristics of MVB *p*-orbital chains inside chalcogenides have been discussed. As the bonding is comprised of partly delocalized electrons across more than two involved atoms, the surface and center of ultrathin films are coupled. Confining such MVB films will thus lead to increased distortions within the film, which are strongest at the surface and gradually approach bulk-like values in the center of the films. As such, the bonding within ultrathin films turns closer to ordinary covalent bonding and the unique properties in the films are suppressed.[51,63,84] This makes material properties tunable by thickness alone, offering a new pathway to property design next to more complex nanostructuring or doping approaches. By comparing the relevant length scales of the confinement effects in theory and experiment, the impact of confinement in theoretical data seems to be underestimated compared to experimental results. While, for example, tight binding calculations based on the bulk unit cells can qualitatively reproduce the blue shift of the peak in the dielectric function, it is apparent that the interplay of confinement and structural distortions needs to be considered adequately to reproduce experimental findings. As the properties of the chalcogenides strongly depend on the degree of distortions, any distortion which is incorporated in the thin film, for exanple, due to vicinity to the surfaces, will alter the properties of the material even in thicknesses, in which "normal" confinement is negligible. In the case of GeSe and SnSe, materials with a covalent bulk structure, confinement effects can instead decrease the distortions in the unit cell.[84] The ultrathin SnSe films are closer to the high symmetry Cmcm phase than their bulk counterpart. This leads to a stronger orbital overlap of the in-plane p orbitals and enables MVB in the film plane. The impact of these changes on the properties of ultrathin SnSe films has, to our knowledge, yet to be measured, but it seems promising to functionalize *p*-bonded covalent chalcogenides with confinement as well.

Recent developments in phase change devices based on ultrathin films were presented in the last section of the article. Two device structures, which use confinement to enhance the device performance of GeTe[105] and Sb_2Te_3[104] have been shown. It becomes apparent that the choice of the interfaces is crucial for the device performance, as it strongly affects the crystallization temperature of the confined films. By choosing different contact materials, the crystallization temperature of GeTe can be decreased into a feasible range, while the amorphous phase of Sb_2Te_3 can be stabilized, as the crystallization temperature is increased.

Experimental studies on the bond rupture behavior by atom probe tomography[109] could provide further insights into the changes in bonding and the interaction with the surrounding materials upon reducing film thickness.[110,111] Such studies

© 2024 The Authors. physica status solidi (a) applications and materials science published by Wiley-VCH GmbH

18626319, 2024, 22, Downloaded from https://onlinelibrary.wiley.com/doi/10.1002/pssa.202300921 by Forschungszentrum Jülich GmbH Research Center, Wiley Online Library on [21/11/2024]. See the Terms and Conditions (https://onlinelibrary.wiley.com/terms-and-conditions) on Wiley Online Library for rules of use; OA articles are governed by the applicable Creative Commons License

can even unravel the impact of grain boundaries on bonding and transport.[10] It is highly desirable to go beyond a characterization of average quantities for the atomic arrangement in thin films and move toward layer-resolved studies. For this goal, TEM seems well-suited, but recent advances in the ease of measuring and analyzing quantitative LEED (I/V curves) also provide interesting alternatives.

While this review only covers mono and sesqui-chalcogenides, some of the methods and ideas involved in the structural characterization of confinement-induced distortions and bond changes could also be transferred to study other materials, which readily exhibit layer-dependent property changes.[112] A detailed study of the interplay of bonding, structure and electronic properties in these heavy TMDCs can help to further classify and understand similarities and differences in more complex electronic systems involving *d*-orbitals.

Acknowledgements

The authors gratefully acknowledge funding from the Deutsche Forschungsgemeinschaft (SFB 917) as well as helpful discussions with Alexander Kiehn. [Correction added on 19 April 2024, after first online publication: the affiliations were attributed correctly in this version.]

Open Access funding enabled and organized by Projekt DEAL.

Conflict of Interest

The authors declare no conflict of interest.

Keywords

chalcogenides, epitaxial growth, metavalent bonding, texture

Received: December 4, 2023
Revised: March 15, 2024
Published online: April 9, 2024

[1] P. Noé, C. Vallée, F. Hippert, F. Fillot, J.-Y. Raty, *Semicond. Sci. Technol.* **2017**, *33*, 013002.
[2] T. Matsunaga, N. Yamada, Y. Kubota, *Acta Crystallogr., Sect. B: Struct. Sci.* **2004**, *60*, 685.
[3] J.-Y. Raty, C. Bichara, C.-F. Schön, C. Gatti, M. Wuttig, *Proc. Natl. Acad. Sci.* **2024**, *121*, e2316498121.
[4] M. Wuttig, C.-F. Schön, J. Lötfering, P. Golub, C. Gatti, J.-Y. Raty, *Adv. Mater.* **2023**, *35*, 2208485.
[5] M. Wuttig, V. L. Deringer, X. Gonze, C. Bichara, J.-Y. Raty, *Adv. Mater.* **2018**, *30*, 1803777.
[6] J.-Y. Raty, M. Schumacher, P. Golub, V. L. Deringer, C. Gatti, M. Wuttig, *Adv.Mater* **2019**, *31*, 1806280.
[7] B. J. Kooi, M. Wuttig, *Adv. Mater.* **2020**, *32*, 1908302.
[8] Y. Yu, D.-S. He, S. Zhang, O. Cojocaru-Mirédin, T. Schwarz, A. Stoffers, X.-Y. Wang, S. Zheng, B. Zhu, C. Scheu, D. Wu, J.-Q. He, M. Wuttig, Z.-Y. Huang, F.-Q. Zu, *Nano Energy* **2017**, *37*, 203.
[9] O. Cojocaru-Mirédin, H. Hollermann, A. M. Mio, A. Y.-T. Wang, M. Wuttig, *J. Phys.: Condens. Matter* **2019**, *31*, 204002.
[10] R. Wu, Y. Yu, S. Jia, C. Zhou, O. Cojocaru-Mirédin, M. Wuttig, *Nat. Commun.* **2023**, *14*, 719.
[11] Y. Yu, C. Zhou, T. Ghosh, C.-F. Schön, Y. Zhou, S. Wahl, M. Raghuwanshi, P. Kerres, C. Bellin, A. Shukla, O. Cojocaru-Mirédin, M. Wuttig, *Adv. Mater.* **2023**, *35*, e2300893.
[12] S. Cecchi, D. Dragoni, D. Kriegner, E. Tisbi, E. Zallo, F. Arciprete, V. Holý, M. Bernasconi, R. Calarco, *Adv. Funct. Mater.* **2019**, *29*, 1805184.
[13] R. E. Simpson, P. Fons, A. V. Kolobov, M. Krbal, J. Tominaga, *Appl. Phys. Lett.* **2012**, *100*, 021911.
[14] G. D'Arrigo, A. M. Mio, J. E. Boschker, A. Meli, S. Cecchi, E. Zallo, A. Sciuto, M. Buscema, E. Bruno, R. Calarco, E. Rimini, *J. Phys. D: Appl. Phys.* **2020**, *53*, 194001.
[15] A. R. Jalil, P. Schüffelgen, H. Valencia, M. Schleenvoigt, C. Ringkamp, G. Mussler, M. Luysberg, J. Mayer, D. Grützmacher, *Nanomaterials* **2023**, *13*, 354.
[16] J. Kampmeier, C. Weyrich, M. Lanius, M. Schall, E. Neumann, G. Mussler, T. Schäpers, D. Grützmacher, *J. Cryst. Growth* **2016**, *443*, 38.
[17] C. Yoo, J. W. Jeon, S. Yoon, Y. Cheng, G. Han, W. Choi, B. Park, G. Jeon, S. Jeon, W. Kim, Y. Zheng, J. Lee, J. Ahn, S. Cho, S. B. Clendenning, I. V. Karpov, Y. K. Lee, J.-H. Choi, C. S. Hwang, *Adv. Mater.* **2022**, *34*, 2207143.
[18] J. Momand, F. R. L. Lange, R. Wang, J. E. Boschker, M. A. Verheijen, R. Calarco, M. Wuttig, B. J. Kooi, *J. Mater. Res.* **2016**, *31*, 3115.
[19] A. M. Mio, S. M. S. Privitera, M. Zimbone, V. Bragaglia, S. Jacobs, C. Persch, F. Arciprete, R. Calarco, M. Wuttig, E. Rimini, *J. Phys. D: Appl. Phys.* **2020**, *53*, 134001.
[20] J. E. Boschker, E. Tisbi, E. Placidi, J. Momand, A. Redaelli, B. J. Kooi, F. Arciprete, R. Calarco, *AIP Adv.* **2017**, *7*, 015106.
[21] J. E. Boschker, L. A. Galves, T. Flissikowski, J. M. J. Lopes, H. Riechert, R. Calarco, *Sci. Rep.* **2015**, *5*, 18079.
[22] R. Wang, J. E. Boschker, E. Bruyer, D. D. Sante, S. Picozzi, K. Perumal, A. Giussani, H. Riechert, R. Calarco, *J. Phys. Chem. C* **2014**, *118*, 29724.
[23] G. Zhang, H. Qin, J. Teng, J. Guo, Q. Guo, X. Dai, Z. Fang, K. Wu, *Appl. Phys. Lett.* **2009**, *95*, 053114.
[24] J. E. Boschker, J. Momand, V. Bragaglia, R. Wang, K. Perumal, A. Giussani, B. J. Kooi, H. Riechert, R. Calarco, *Nano Lett.* **2014**, *14*, 3534.
[25] A. Giussani, K. Perumal, M. Hanke, P. Rodenbach, H. Riechert, R. Calarco, *Phys. Status Solidi B* **2012**, *249*, 1939.
[26] F. Arciprete, J. E. Boschker, S. Cecchi, E. Zallo, V. Bragaglia, R. Calarco, *Adv. Mater. Interfaces* **2022**, *9*, 2101556.
[27] M. Schuck, S. Rieß, M. Schreiber, G. Mussler, D. Grützmacher, H. Hardtdegen, *J. Cryst. Growth* **2015**, *420*, 37.
[28] S. Borisova, J. Krumrain, M. Luysberg, G. Mussler, D. Grützmacher, *Cryst. Growth Des.* **2012**, *12*, 6098.
[29] Yu. S. Zaytseva, N. I. Borgardt, A. S. Prikhodko, E. Zallo, R. Calarco, *Semiconductors* **2021**, *55*, 1033.
[30] Y. Zhang, K. He, C.-Z. Chang, C.-L. Song, L.-L. Wang, X. Chen, J.-F. Jia, Z. Fang, X. Dai, W.-Y. Shan, S.-Q. Shen, Q. Niu, X.-L. Qi, S.-C. Zhang, X.-C. Ma, Q.-K. Xue, *Nat. Phys.* **2010**, *6*, 584.
[31] M. Fang, Z. Wang, H. Gu, M. Tong, B. Song, X. Xie, T. Zhou, X. Chen, H. Jiang, T. Jiang, S. Liu, *Appl. Surf. Sci.* **2020**, *509*, 144822.
[32] M. Neupane, A. Richardella, J. Sánchez-Barriga, S. Xu, N. Alidoust, I. Belopolski, C. Liu, G. Bian, D. Zhang, D. Marchenko, A. Varykhalov, O. Rader, M. Leandersson, T. Balasubramanian, T.-R. Chang, H.-T. Jeng, S. Basak, H. Lin, A. Bansil, N. Samarth, M. Z. Hasan, *Nat. Commun.* **2014**, *5*, 3841.
[33] G. Wang, X. Zhu, J. Wen, X. Chen, K. He, L. Wang, X. Ma, Y. Liu, X. Dai, Z. Fang, J. Jia, Q. Xue, *Nano Res.* **2010**, *3*, 874.
[34] B. Croes, F. Cheynis, Y. Fagot-Revurat, P. Müller, S. Curiotto, F. Leroy, *Phys. Rev. Mater.* **2023**, *7*, 014409.

© 2024 The Authors. physica status solidi (a) applications and materials science published by Wiley-VCH GmbH

18626319, 2024, 22, Downloaded from https://onlinelibrary.wiley.com/doi/10.1002/pssa.202300921 by Forschungszentrum Jülich GmbH Research Center, Wiley Online Library on [21/11/2024]. See the Terms and Conditions (https://onlinelibrary.wiley.com/terms-and-conditions) on Wiley Online Library for rules of use; OA articles are governed by the applicable Creative Commons License

[35] I. Hilmi, A. Lotnyk, J. W. Gerlach, P. Schumacher, B. Rauschenbach, *APL Mater.* **2017**, *5*, 050701.
[36] P. A. Vermeulen, J. Mulder, J. Momand, B. J. Kooi, *Nanoscale* **2018**, *10*, 1474.
[37] I. Hilmi, A. Lotnyk, J. W. Gerlach, P. Schumacher, B. Rauschenbach, *Mater. Des.* **2019**, *168*, 107657.
[38] H. Zhang, D. T. Yimam, S. de Graaf, J. Momand, P. A. Vermeulen, Y. Wei, B. Noheda, B. J. Kooi, *ACS Nano* **2021**, *15*, 2869.
[39] M. Behrens, A. Lotnyk, J. W. Gerlach, M. Ehrhardt, P. Lorenz, B. Rauschenbach, *ACS Appl. Mater. Interfaces* **2019**, *11*, 41544.
[40] F. Hippert, P. Kowalczyk, N. Bernier, C. Sabbione, X. Zucchi, D. Térébénec, C. Mocuta, P. Noé, *J. Phys. D: Appl. Phys.* **2020**, *53*, 154003.
[41] M. M. Dück, T. Schäfer, S. Jakobs, C.-F. Schön, H. Niehaus, O. Cojocaru-Mirédin, M. Wuttig, *Phys. Status Solidi RRL* **2019**, *13*, 1800578.
[42] J. E. Boschker, R. Calarco, *Adv. Phys.: X* **2017**, *2*, 675.
[43] H. Hardtdegen, M. Mikulics, S. Rieß, M. Schuck, T. Saltzmann, U. Simon, M. Longo, *Prog. Cryst. Growth Charact. Mater.* **2015**, *61*, 27.
[44] Y. K. Lee, C. Yoo, W. Kim, J. W. Jeon, C. S. Hwang, *J. Mater. Chem. C* **2021**, *9*, 3708.
[45] D. M. Többens, N. Stüßer, K. Knorr, H. M. Mayer, G. Lampert, *Mater. Sci. Forum* **2001**, *378–381*, 288.
[46] T. Nonaka, G. Ohbayashi, Y. Toriumi, Y. Mori, H. Hashimoto, *Thin Solid Films* **2000**, *370*, 258.
[47] M. Küpers, R. P. Stoffel, B. Bong, M. G. Herrmann, Z. Li, A. Meledin, J. Mayer, K. Friese, R. Dronskowski, *Z. Naturforsch., B* **2020**, *75*, 41.
[48] R. Wang, W. Zhang, J. Momand, I. Ronneberger, J. E. Boschker, R. Mazzarello, B. J. Kooi, H. Riechert, M. Wuttig, R. Calarco, *NPG Asia Mater.* **2017**, *9*, e396.
[49] J. Momand, J. E. Boschker, R. Wang, R. Calarco, B. J. Kooi, *CrystEngComm* **2018**, *20*, 340.
[50] G. J. Pietsch, U. Köhler, M. Henzler, *J. Vac. Sci. Technol., B: Microelectron. Nanometer Struct. –Process., Meas., Phenom.* **1994**, *12*, 78.
[51] P. Kerres, Y. Zhou, H. Vaishnav, M. Raghuwanshi, J. Wang, M. Häser, M. Pohlmann, Y. Cheng, C.-F. Schön, T. Jansen, C. Bellin, D. E. Bürgler, A. R. Jalil, C. Ringkamp, H. Kowalczyk, C. M. Schneider, A. Shukla, M. Wuttig, *Small* **2022**, *18*, 2201753.
[52] H. Hardtdegen, S. Rieß, M. Schuck, K. Keller, P. Jost, H. Du, M. Bornhöfft, A. Schwedt, G. Mussler, M. V. D. Ahe, J. Mayer, G. Roth, D. Grützmacher, M. Mikulics, *J. Alloys Compd.* **2016**, *679*, 285.
[53] I. Hilmi, A. Lotnyk, J. W. Gerlach, P. Schumacher, B. Rauschenbach, *Mater. Des.* **2017**, *115*, 138.
[54] U. Ross, A. Lotnyk, E. Thelander, B. Rauschenbach, *J. Alloys Compd.* **2016**, *676*, 582.
[55] F. Lüpke, S. Just, G. Bihlmayer, M. Lanius, M. Luysberg, J. Doležal, E. Neumann, V. Cherepanov, I. Ošt'ádal, G. Mussler, D. Grützmacher, B. Voigtländer, *Phys. Rev. B* **2017**, *96*, 035301.
[56] D. Dragoni, *Phys. Rev. B* **2022**, *106*, 195427.
[57] Y. Saito, P. Fons, L. Bolotov, N. Miyata, A. V. Kolobov, J. Tominaga, *AIP Adv.* **2016**, *6*, 045220.
[58] S. Raoux, J. L. Jordan-Sweet, A. J. Kellock, *J. Appl. Phys.* **2008**, *103*, 114310.
[59] R. Wang, F. R. L. Lange, S. Cecchi, M. Hanke, M. Wuttig, R. Calarco, *Adv. Funct. Mater.* **2018**, *28*, 1705901.
[60] A. M. Mio, P. M. Konze, A. Meledin, M. Küpers, M. Pohlmann, M. Kaminski, R. Dronskowski, J. Mayer, M. Wuttig, *Adv. Funct. Mater.* **2019**, *29*, 1902332.
[61] W. Zhang, H. Zhang, S. Sun, X. Wang, Z. Lu, X. Wang, J.-J. Wang, C. Jia, C.-F. Schön, R. Mazzarello, E. Ma, M. Wuttig, *Adv. Sci.* **2023**, *10*, 2300901.
[62] J. Hempelmann, P. C. Müller, C. Ertural, R. Dronskowski, *Angew. Chem., Int. Ed.* **2022**, *61*, e202115778.
[63] J. Mertens, P. Kerres, Y. Xu, M. Raghuwanshi, D. Kim, C.-F. Schön, J. Frank, F. Hoff, Y. Zhou, R. Mazzarello, A. R. Jalil, M. Wuttig, *Adv. Funct. Mater.* **2024**, *34*, 2307681.
[64] G. V. Pushkarev, V. G. Mazurenko, V. V. Mazurenko, D. W. Boukhvalov, *J. Phys. Chem. C* **2023**, *127*, 8148.
[65] M. Rimoldi, R. Cecchini, C. Wiemer, E. Longo, S. Cecchi, R. Mantovan, M. Longo, *Cryst. Growth Des.* **2021**, *21*, 5135.
[66] M. Rimoldi, R. Cecchini, C. Wiemer, A. Lamperti, E. Longo, L. Nasi, L. Lazzarini, R. Mantovan, M. Longo, *RSC Adv.* **2020**, *10*, 19936.
[67] D. T. Yimam, M. Ahmadi, B. J. Kooi, *Mater. Today Nano* **2023**, *23*, 100365.
[68] Y. Saito, P. Fons, A. V. Kolobov, J. Tominaga, *Phys. Status Solidi B* **2015**, *252*, 2151.
[69] M. W. Chase, N. I. S. Organization (US), *NIST-JANAF Thermochemical Tables*, American Chemical Society, Washington, DC **1998**.
[70] M. Aspiala, D. Sukhomlinov, P. Taskinen, *Solid State Ionics* **2014**, *265*, 80.
[71] E. H. P. Cordfunke, W. Ouweltjes, G. Prins, *J. Chem. Thermodyn.* **1987**, *19*, 369.
[72] J. Cox, D. Wagman, V. Medvedev, in *CODATA Key Values for Thermodynamics*, Hemisphere Publishing Corp., New York, NY **1989**.
[73] M. Behrens, A. Lotnyk, J. W. Gerlach, I. Hilmi, T. Abel, P. Lorenz, B. Rauschenbach, *Nanoscale* **2018**, *10*, 22946.
[74] I. Ronneberger, W. Zhang, R. Mazzarello, *MRS Commun.* **2018**, *8*, 1018.
[75] Y. Xu, Y. Zhou, X.-D. Wang, W. Zhang, E. Ma, V. L. Deringer, R. Mazzarello, *Adv. Mater.* **2022**, *34*, 2109139.
[76] Y. Zhou, W. Zhang, E. Ma, V. L. Deringer, *Nat. Electron.* **2023**, *6*, 746.
[77] R. E. Peierls, *Quantum Theory of Solids*, Clarendon Press, Oxford **1955**.
[78] J.-Y. Raty, M. Wuttig, *J. Phys. D: Appl. Phys.* **2020**, *53*, 234002.
[79] K. L. I. Kobayashi, Y. Kato, Y. Katayama, K. F. Komatsubara, *Phys. Rev. Lett.* **1976**, *37*, 772.
[80] C. Bellin, A. Pawbake, L. Paulatto, K. Béneut, J. Biscaras, C. Narayana, A. Polian, D. J. Late, A. Shukla, *Phys. Rev. Lett.* **2020**, *125*, 145301.
[81] K. Chang, T. P. Kaloni, H. Lin, A. Bedoya-Pinto, A. K. Pandeya, I. Kostanovskiy, K. Zhao, Y. Zhong, X. Hu, Q.-K. Xue, X. Chen, S.-H. Ji, S. Barraza-Lopez, S. S. P. Parkin, *Adv. Mater.* **2019**, *31*, 1804428.
[82] K. Chang, J. Liu, H. Lin, N. Wang, K. Zhao, A. Zhang, F. Jin, Y. Zhong, X. Hu, W. Duan, Q. Zhang, L. Fu, Q.-K. Xue, X. Chen, S.-H. Ji, *Science* **2016**, *353*, 274.
[83] T. P. Kaloni, K. Chang, B. J. Miller, Q.-K. Xue, X. Chen, S.-H. Ji, S. S. P. Parkin, S. Barraza-Lopez, *Phys. Rev. B* **2019**, *99*, 134108.
[84] I. Ronneberger, Z. Zanolli, M. Wuttig, R. Mazzarello, *Adv. Mater.* **2020**, *32*, 2001033.
[85] A. K. Deb, V. Kumar, *Phys. Status Solidi B* **2017**, *254*, 1600379.
[86] F. Xue, Z. Zhao, Y. Zhang, T. Liu, Y. Lu, J. Zhang, *Phys. Rev. B* **2022**, *106*, 104301.
[87] V. L. Deringer, M. Lumeij, R. Dronskowski, *J. Phys. Chem. C* **2012**, *116*, 15801.
[88] B. B. Haidet, L. Nordin, A. J. Muhowski, K. D. Vallejo, E. T. Hughes, J. Meyer, P. J. Simmonds, D. Wasserman, K. Mukherjee, *J. Vac. Sci. Technol., A* **2021**, *39*, 023404.
[89] B. B. Haidet, E. T. Hughes, K. Mukherjee, *Phys. Rev. Mater.* **2020**, *4*, 033402.
[90] S. Maier, S. Steinberg, Y. Cheng, C.-F. Schön, M. Schumacher, R. Mazzarello, P. Golub, R. Nelson, O. Cojocaru-Mirédin, J.-Y. Raty, M. Wuttig, *Adv. Mater.* **2020**, *32*, 2005533.

© 2024 The Authors. physica status solidi (a) applications and materials science published by Wiley-VCH GmbH

18626319, 2024, 22, Downloaded from https://onlinelibrary.wiley.com/doi/10.1002/pssa.202300921 by Forschungszentrum Jülich GmbH Research Center, Wiley Online Library on [21/11/2024]. See the Terms and Conditions (https://onlinelibrary.wiley.com/terms-and-conditions) on Wiley Online Library for rules of use; OA articles are governed by the applicable Creative Commons License

[91] R. Wang, D. Campi, M. Bernasconi, J. Momand, B. J. Kooi, M. A. Verheijen, M. Wuttig, R. Calarco, *Sci. Rep.* **2016**, *6*, 32895.
[92] Y. Wang, S. Huang, B. Raji-Adefila, A. Outka, J.-H. Wang, D. Chen, *J. Am. Chem. Soc.* **2022**, *144*, 19838.
[93] M. Kaminski, M. Wuttig, R. Waser, *Phase Change Superlattices and Thin Film Effects: MBE-Growth and Characterization*, RWTH Aachen University, Aachen **2020**.
[94] R. Dingle, W. Wiegmann, C. H. Henry, *Phys. Rev. Lett.* **1974**, *33*, 827.
[95] G. Allan, C. Delerue, *Phys. Rev. B* **2004**, *70*, 245321.
[96] L. Guarneri, S. Jakobs, A. von Hoegen, S. Maier, M. Xu, M. Zhu, S. Wahl, C. Teichrib, Y. Zhou, O. Cojocaru-Mirédin, M. Raghuwanshi, C.-F. Schön, M. Drögeler, C. Stampfer, R. P. S. M. Lobo, A. Piarristeguy, A. Pradel, J.-Y. Raty, M. Wuttig, *Adv. Mater.* **2021**, *33*, 2102356.
[97] D. T. Yimam, B. J. Kooi, *ACS Appl. Mater. Interfaces* **2022**, *14*, 13593.
[98] Z. Cheng, T. Milne, P. Salter, J. S. Kim, S. Humphrey, M. Booth, H. Bhaskaran, *Sci. Adv.* **2021**, *7*, eabd7097.
[99] M. J. Polking, J. J. Urban, D. J. Milliron, H. Zheng, E. Chan, M. A. Caldwell, S. Raoux, C. F. Kisielowski, J. W. Ager, R. Ramesh, A. P. Alivisatos, *Nano Lett.* **2011**, *11*, 1147.
[100] J. Zhang, Z. Peng, A. Soni, Y. Zhao, Y. Xiong, B. Peng, J. Wang, M. S. Dresselhaus, Q. Xiong, *Nano Lett.* **2011**, *11*, 2407.
[101] F. Wang, L. Li, W. Huang, L. Li, B. Jin, H. Li, T. Zhai, *Adv. Funct. Mater.* **2018**, *28*, 1802707.
[102] E. Zallo, D. Dragoni, Y. Zaytseva, S. Cecchi, N. I. Borgardt, M. Bernasconi, R. Calarco, *Phys. Status Solidi RRL* **2021**, *15*, 2000434.
[103] M. Salinga, B. Kersting, I. Ronneberger, V. P. Jonnalagadda, X. T. Vu, M. Le Gallo, I. Giannopoulos, O. Cojocaru-Mirédin, R. Mazzarello, A. Sebastian, *Nat. Mater.* **2018**, *17*, 681.
[104] K. Ding, B. Chen, F. Rao, *Mater. Sci. Semicond. Process.* **2021**, *134*, 105999.
[105] Y. Meng, Y. Chen, K. Peng, B. Chen, C. Gu, Y. Gao, G. Wang, X. Shen, *AIP Adv.* **2023**, *13*, 035205.
[106] S. Raoux, H.-Y. Cheng, J. L. Jordan-Sweet, B. Muñoz, M. Hitzbleck, *Appl. Phys. Lett.* **2009**, *94*, 183114.
[107] A. I. Khan, X. Wu, C. Perez, B. Won, K. Kim, P. Ramesh, H. Kwon, M. C. Tung, Z. Lee, I.-K. Oh, K. Saraswat, M. Asheghi, K. E. Goodson, H.-S. P. Wong, E. Pop, *Nano Lett.* **2022**, *22*, 6285.
[108] K. Aryana, J. T. Gaskins, J. Nag, D. A. Stewart, Z. Bai, S. Mukhopadhyay, J. C. Read, D. H. Olson, E. R. Hoglund, J. M. Howe, A. Giri, M. K. Grobis, P. E. Hopkins, *Nat. Commun.* **2021**, *12*, 774.
[109] B. Gault, A. Chiaramonti, O. Cojocaru-Mirédin, P. Stender, R. Dubosq, C. Freysoldt, S. K. Makineni, T. Li, M. Moody, J. M. Cairney, *Nat. Rev. Methods Primers* **2021**, *1*, 51.
[110] C. Rodenkirchen, M. Cagnoni, S. Jakobs, Y. Cheng, J. Keutgen, Y. Yu, M. Wuttig, O. Cojocaru-Mirédin, *Adv. Funct. Mater.* **2020**, *30*, 1910039.
[111] M. Zhu, O. Cojocaru-Mirédin, A. M. Mio, J. Keutgen, M. Küpers, Y. Yu, J.-Y. Cho, R. Dronskowski, M. Wuttig, *Adv. Mater.* **2018**, *30*, 1706735.
[112] H. Ma, P. Chen, B. Li, J. Li, R. Ai, Z. Zhang, G. Sun, K. Yao, Z. Lin, B. Zhao, R. Wu, X. Tang, X. Duan, X. Duan, *Nano Lett.* **2018**, *18*, 3523.
[113] J. Momand, R. Wang, J. E. Boschker, M. A. Verheijen, R. Calarco, B. J. Kooi, *Nanoscale* **2017**, *9*, 8774.
[114] J. E. Boschker, M. Boniardi, A. Redaelli, H. Riechert, R. Calarco, *Appl. Phys. Lett.* **2015**, *106*, 023117.
[115] A. I. Khan, H. Kwon, R. Islam, C. Perez, M. E. Chen, M. Asheghi, K. E. Goodson, H.-S. P. Wong, E. Pop, *IEEE Electron Device Lett.* **2020**, *41*, 1657.
[116] K. Ding, J. Wang, Y. Zhou, H. Tian, L. Lu, R. Mazzarello, C. Jia, W. Zhang, F. Rao, E. Ma, *Science* **2019**, *366*, 210.
[117] J. Y. Wu, Y. S. Chen, W. S. Khwa, S. M. Yu, T. Y. Wang, J. C. Tseng, Y. D. Chih, C. H. Diaz, in *2018 IEEE Int. Electron Devices Meeting (IEDM)*, IEEE, Piscataway, NJ **2018**, pp. 27.6.1–27.6.4.
[118] M. He, D. He, H. Qian, Q. Lin, D. Wan, X. Cheng, M. Xu, H. Tong, X. Miao, *IEEE Electron Device Lett.* **2019**, *40*, 1595.
[119] F. Xiong, M.-H. Bae, Y. Dai, A. D. Liao, A. Behnam, E. A. Carrion, S. Hong, D. Ielmini, E. Pop, *Nano Lett.* **2013**, *13*, 464.
[120] S. Kim, N. Sosa, M. BrightSky, D. Mori, W. Kim, Y. Zhu, K. Suu, C. Lam, in *2013 IEEE Int. Electron Devices Meeting*, IEEE, Piscataway, NJ **2013**, pp. 30.7.1–30.7.4.
[121] A. Kiouseloglou, G. Navarro, V. Sousa, A. Persico, A. Roule, A. Cabrini, G. Torelli, S. Maitrejean, G. Reimbold, B. De Salvo, F. Clermidy, L. Perniola, *IEEE Trans. Electron Devices* **2014**, *61*, 1246.
[122] S. Ghazi Sarwat, T. M. Philip, C.-T. Chen, B. Kersting, R. L. Bruce, C.-W. Cheng, N. Li, N. Saulnier, M. BrightSky, A. Sebastian, *Adv. Funct. Mater.* **2021**, *31*, 2106547.
[123] H.-S. P. Wong, C. Ahn, M. Beauchamp, J. Cao, H.-Y. Chen, W. C. Chen, S. B. Eryilmaz, S. W. Fong, W. Hwang, J. A. Incorvia, R. Islam, Z. Jiang, H. Li, S. Liu, C. Neumann, K. Okabe, S. Qin, Y. C. Shen, M. Shi, J. Sohn, M. Tung, W. Wan, X. Wu, Y. Wu, S. Yu, Z. Yu, X. Zheng, https://nano.stanford.edu/stanford-memory-trends (accessed: June 2022).

Peter Kerres received his M.Sc. in experimental condensed matter physics from RWTH Aachen University, Germany in 2018, where is pursuing his Ph.D. in physics in the group of Matthias Wuttig at the 1st Institute of Physics(IA). Since 2022, he is working as a group leader in the PGI 10, Forschungszentrum Jülich. His research is focused on growth and structural characterization of textured chalcogenides and resistive switching.

© 2024 The Authors. physica status solidi (a) applications and materials science published by Wiley-VCH GmbH

18626319, 2024, 22, Downloaded from https://onlinelibrary.wiley.com/doi/10.1002/pssa.202300921 by Forschungszentrum Jülich GmbH Research Center, Wiley Online Library on [21/11/2024]. See the Terms and Conditions (https://onlinelibrary.wiley.com/terms-and-conditions) on Wiley Online Library for rules of use; OA articles are governed by the applicable Creative Commons License

Matthias Wuttig received his Ph.D. in physics in 1988 from RWTH Aachen/Forschungszentrum Jülich. He was a visiting professor at several institutions including Lawrence Berkeley Laboratory, CINaM (Marseille), Stanford University, Hangzhou University, IBM Almaden, Bell Labs, DSI in Singapore, and the Chinese Academy of Sciences in Shanghai. In 1997, he was appointed full professor at RWTH Aachen. From 2011 until 2023, he has been heading a collaborative research center on resistively switching chalcogenides, funded by the DFG. He has written about 440 papers with over 30.000 citations (Web of Science) and won several awards and recognitions, including an ERC Advanced Grant.

© 2024 The Authors. physica status solidi (a) applications and materials science published by Wiley-VCH GmbH

18626319, 2024, 22, Downloaded from https://onlinelibrary.wiley.com/doi/10.1002/pssa.202300921 by Forschungszentrum Jülich GmbH Research Center, Wiley Online Library on [21/11/2024]. See the Terms and Conditions (https://onlinelibrary.wiley.com/terms-and-conditions) on Wiley Online Library for rules of use; OA articles are governed by the applicable Creative Commons License